CZECH TECHNICAL UNIVERSITY IN PRAGUE

Faculty of Nuclear Sciences and Physical Engineering

Department of Physics

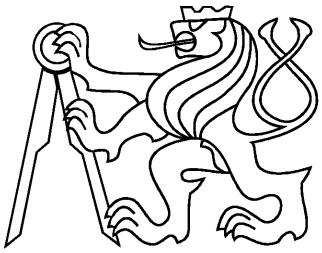

Bachelor thesis

Antimatter production in nucleus-nucleus collisions

Jana Crkovská

Supervisor: Mgr. Jaroslav Bielčík, Ph.D.

Prague, 2012

ČESKÉ VYSOKÉ UČENÍ TECHNICKÉ
V PRAZE
Fakulta Jaderná a Fyzikálně Inženýrská
Katedra Fyziky

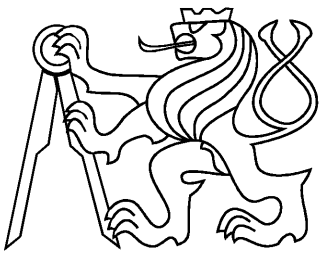

Bakalářská práce

Produkce antihmoty v jádro-jaderných srážkách

Jana Crkovská

Vedoucí práce: Mgr. Jaroslav Bielčík, Ph.D.

Praha, 2012

Prohlášení:

Prohlašuji, že jsem svou bakalářskou práci vypracovala samostatně a použila jsem pouze podklady (literaturu, software, atd.) uvedené v přiloženém seznamu.

Nemám závažný důvod proti užití tohoto školního díla ve smyslu 60 Zákona .121/2000 Sb., o právu autorském, o právech souvisejících s právem autorským a o změně některých zákonů (autorský zákon).

V Praze dne 9.července 2012

Jana Crkovská

Title:
Antimatter production in nucleus-nucleus collisions

Author: Jana Crkovská

Specialization: Experimental nuclear physics

Sort of project: Bachelor's thesis

Supervisor: Mgr. Jaroslav Bielčík, Ph.D.

Abstract: Relativistic nucleus-nucleus collisions provide an unique tool to investigate nuclear matter at extreme conditions. The primary goal of the physics programme of the relativistic heavy-ion collisions investigations is study of the quark-gluon plasma. However, new forms of matter and antimatter are created during such collisions, which can be further investigated. Production of nuclei of antihelium and antihypertriton was recently reported by STAR. This thesis discusses the discoveries together with related subjects of antimatter, CP-violation and hypernuclei production.

Key words: Antimatter, heavy-ion collisions, STAR, antihelium, antihypertriton.

Název práce:
Produkce antihmoty v jádro-jaderných srážkách

Autor: Jana Crkovská

Zaměření: Experimentální jaderná fyzika

Druh práce: Bakalářská práce

Vedoucí práce: Mgr. Jaroslav Bielčík, Ph.D.

Abstrakt: Relativistické srážky těžkých jader umožňují studium jaderné hmoty při extrémních podmínkách. Prvotním cílem těchto srážek je studium kvark-gluonového plazmatu. Jelikož při nich dochází ke vzniku velkého množství hmoty i antihmoty, umožňují tak mimo jiné pozorování nových druhů antičástic. Vznik jader antihelia a antihypertritonu byl nedávno pozorován zařízením STAR na RHIC. Tato práce shrnuje tyto objevy společně s přidruženými tématy, jako jsou např. antihmota, narušení CP symetrie a produkce hyperjader.

Klíčová slova: Antihmota, relativistické srážky iontů, STAR, antihelium, antihypertriton.

Acknowledgement

I would like to express my gratitude to all those who supported me during my work on this thesis. I am very grateful to Mgr. Jaroslav Bielčík, Ph.D. for his invaluable help and advice.

Jana Crkovská

Contents

List of Figures

List of Tables

Preface

Relativistic heavy-ion collisions provide a unique tool to study nuclear matter at extreme conditions. During such collisions, huge amounts of energy are released, from which many forms of matter and antimatter are born. From investigation of heavy-ion collisions, we can acquire knowledge of a new state of matter – the quark-gluon plasma. The quark-gluon plasma is is a state of matter where quarks and gluons, normally confined inside nucleons, are deconfined. Such state is predicted to be reached at high energies and densities. Since such extreme conditions existed in the brief period of time shortly after the Big Bang, study of properties of quark-gluon plasma can tell us more about the early history of the Universe.

The antimatter was predicted by P. A. M. Dirac in 1931. Its existence was confirmed two years later with discovery of antielectron – the positron. Since then, many new forms of antimatter were observed. High-energy antiparticles are commonly observed and used in experiments these days, positrons are even used regularly in medicine – in the technique of positron emission therapy.

This thesis discusses several topics related to recent discovery of antihelium and antihypertriton in heavy-ion collisions at the Relativistic Heavy-Ion Collider at Brookhaven National Laboratory, USA. The first chapter presents a general overview of particle physics and introduces topics related to antimatter. The first discoveries of antiparticles (namely positron, antiproton and antineutron) as well as discovery of antihydrogen are discussed in Chapter 2. The following part contains basic information about hypernuclei. Hypernucleus is a nucleus which contains one or more strange baryons – hyperons. Hyperons are baryons composed of at least one strange quark. Since RHIC is not the only facility to inspect antimatter, experiments with antihydrogen ALPHA and AEg̅IS carried at CERN are presented in Chapter 4, ALPHA inspects the spectrum of antihydrogen atom. It is expected that the spectra of hydrogen and antihydrogen are identical. AEg̅IS will investigate impact of Earth's local gravitational field on antimatter. In the last chapter, the STAR detector at RHIC is presented. Recently, STAR reported evidence of production of the $^{4}\overline{\mathrm{He}}$ antihelium, the heaviest antinuclei so far observed. Another significant discovery is that of the $^{3}_{\Lambda}\overline{\mathrm{H}}$ antihypertriton. The chapter is concluded with future outlook for STAR.

Chapter 1

Introduction to elementary particles

The aim of this chapter is to introduce the reader to elementary particle physics. Particle physics studies structure of the world on the finest level – smaller than atoms, even smaller than protons and neutrons that form nuclei. Main sources for this chapter are books [1] and [2].

1.1 Particle classification

There are two common ways to classify elementary particles. The first groups the particles with respect to their spin to and classifies them as bosons or fermions. The other one divides them into two groups, quarks and leptons, according to interactions the particles are subjected to.

1.1.1 Spin-statistic theorem

Elementary particles can be divided into two main groups according to their intrinsic spin: bosons, with an integer spin, and fermions, bearing a half-integer spin. Spin of a particle is usually given in units of $\hbar$.[1] This classification is particularly useful when describing a system of identical particles. The system of identical bosons can be described with a symmetric wave function. When two particles of the system (particle 1 and 2) are interchanged, the wave function does not change sign:

$$\psi(1;2) = \psi(2;1) \tag{1.1}$$

On the other hand, the system of identical fermions would be described by an antisymmetrical wave function. The wave function then changes sign when two

[1] The reduced Planck constant $\hbar$ is related to Planck constant h by $h = 2\pi\hbar$. The Planck constant reflects the size of energy quantum, $\hbar = 6.582 \cdot 10^{-22}$ MeVs $= 1.054 \cdot 10^{-34}$ Js. Value taken from [1].

particles are switched:

$$\psi(1;2) = -\psi(2;1) \tag{1.2}$$

As a result, fermions do obey Pauli's exclusion principle, while bosons do not [3]. According to Pauli's exclusion principle, two fermions cannot occupy the same state simultaneously.

Let ψ of each particle be a function of coordinates and projection of spin to the z-axis: $\psi(\eta_i) \equiv \psi(\vec{r}; s_z); i = 1, 2$. Suppose the two particles are in the same state: $\eta_1 = \eta_2$. Then according to (1.1), by changing the particles in the system described by $\psi(\eta_1; \eta_1)$ we obtain again $\psi(\eta_1; \eta_1)$. On the other hand, for $\eta_1 = \eta_2$ (1.2) gives

$$\psi(\eta_1; \eta_1) = 0$$

Therefore one state can be occupied only and only by one fermion.

1.1.2 Quarks and leptons

All the matter that we know is constituted from quarks and leptons. However, astrophysical observations indicate that all these particles represent only 4% of all the matter in the Universe. Both quarks and leptons are truly elementary particles, since they are both considered to be point-like. Both carry spin of $1/2\hbar$ which means they are fermions.

Leptons interact only electro-weakly. They can be either charged or neutral. There are three possible types, *flavours*, of charged leptons: electron, muon μ and tauon τ.

The neutral leptons, neutrinos, can be grouped with charged leptons of equal flavour, e. g. the neutrino emitted with electron in β-decay is the electron-neutrino ν_e.

All charged leptons can exist in two forms: left-handed, with spin projection to the momentum axis $s_z = -1/2\hbar$, and right-handed, with $s_z = +1/2\hbar$. Neutrino, on the other hand, occurs only in the left-handed form while the antineutrino is always right-handed.

Quarks do interact electro-weakly. In addition, they are subjected to the strong interaction. Quarks also do have an additional degree of freedom, which is, as in the case of leptons, flavour. Altogether, there are six quark flavours, which again can be arranged to three doublets. The doublets (c, s) and (t, b) are heavier analogies of the doublet (u, d).

Since no free quarks were ever observed, it is assumed, that, at normal energies, they do always form bound states. Such quark complexes are called hadrons and we distinguish two different kinds: baryons, consisting of three quarks or three antiquarks, and mesons, formed by quark-antiquark pair. Few examples can be found in Table 1.2. However, at sufficiently high energies, hadrons should undergo a phase transition into a state at which quarks and gluons are free. This state is called *quark-gluon plasma* (QGP).

particle	charge [e]	mass [GeV/c^2]	particle	charge [e]	mass [GeV/c^2]
e	-1	$0.511 \cdot 10^{-3}$	u	+2/3	$2.4 \cdot 10^{-3}$
ν_e	0	$< 3 \cdot 10^{-9}$	d	-1/3	$4.8 \cdot 10^{-3}$
μ	-1	0.10566	c	+2/3	1.27
ν_μ	0	$< 0.19 \cdot 10^{-3}$	s	-1/3	0.104
τ	-1	1.784	t	+2/3	171.2
ν_τ	0	$< 18 \cdot 10^{-3}$	b	-1/3	4.2

Table 1.1: List of leptons and quarks, each with respective charge and mass. Both groups are divided into three subgroups called *generations*. Taken from Ref. [1].

Baryons		Mesons	
particle	quark composition	particle	quark composition
proton	uud	π^-	$u\bar{d}$
neutron	udd	π^+	$d\bar{u}$
Λ	uds	π^0	$(u\bar{u} - d\bar{d})/\sqrt{2}$
Δ^{++}	uuu	K^0	$d\bar{s}$

Table 1.2: Examples of hadrons and their quark composition [4].

Nowadays, common matter on Earth is formed solely of u and d quarks. Heavier quarks are produced only in collisions at accelerators or from interactions of cosmic rays with the atmosphere. Once formed, they tend to decay quickly into u or d quark. Even though heavier quarks may also form bound states, these are highly unstable due to short lifetime of their quarks.

1.2 Fundamental interactions

There are four fundamental interactions through which elementary particles can interact : electromagnetic, strong, weak and gravitational. During all of these processes, momentum is exchanged between the particle via the exchange of boson mediators. These are photon, gluon, bosons $W^\pm$ and Z^0 and graviton respectively.

Electromagnetic interaction occurs between all electrically charged particles, even at long distances. The corresponding field particle is a *photon*, with zero mass and spin $1\hbar$. The electromagnetic force bounds electrons with nuclei to form atoms, bounds atoms within molecules and single molecules in matter.

Weak interaction takes place between all quarks and leptons. It is brought about by exchange of *weak bosons* $W^{\pm}$ and Z^0 of mass 80 GeV/c^2 and 90 GeV/c^2 respectively. Both carry spin $1\hbar$. The range of the weak interaction is limited to 10^{-18} m due to the relatively huge mass of its field particles. The weak interaction can change flavours of quarks and leptons.

Strong interaction occurs only between quarks. It is the strongest of all four interactions, hence its name (for details, please see Table 1.3). The range is limited up to 10^{-15} m. The quarks carry *colour charge* (red, green or blue). The interaction is mediated by *gluons*. Gluons are massless, with spin $1\hbar$ and they carry both colour and anticolour. There are 8 gluons in total: $R\bar{B}$, $R\bar{G}$, $B\bar{G}$, $B\bar{R}$, $G\bar{R}$, $G\bar{B}$, $1/\sqrt{2}(R\bar{R}-B\bar{B})$ and $1/\sqrt{6}(R\bar{R}+B\bar{B}-2G\bar{G})$, where R, G, B denotes red, green and blue charge respectively. Strong interaction is responsible for binding quarks in hadrons and for binding nucleons in nuclei. The hadrons are always *white* - meaning any baryon must contain one quark or antiquark of each colour, mesons contain the quark-antiquark pair of the same colour. Quarks have an extra degree of freedom due to the colour charge. Existence of baryons composed of three quarks of same colour would be otherwise impossible due to Pauli's exclusion principle. However, such baryons have been observed. As an example we can list Δ^{++} (uuu).

Gravitational interaction affects all matter and radiation. Its predicted field particle is *graviton*, of zero mass and spin $2\hbar$. Gravitation is usually neglected on subatomic scale - it's relative magnitude compared to other interactions is more than thirty times smaller (see Table 1.3).

Examples of strong, weak and electromagnetic forces are shown in Fig. 1.1. Characteristics of all four fundamental interactions are summed up in Table 1.3.

interaction	electromagnetic	weak	strong	gravitational
range [m]	∞	10^{-18}	$\leq 10^{-15}$	∞
mean life-time [s]	10^{-20}	10^{-10}	10^{-23}	—
relative strength	10^{-2}	10^{-7}	1	10^{-39}
boson intermediator	photon	$W^{\pm}$, Z^0	gluon	graviton
spin [$\hbar$]	1	1	1	2
mass [GeV/c^2]	0	80.2, 91	0	0

Table 1.3: Characteristics of fundamental interactions. The relative strength of each interaction compares its magnitude to the magnitude of the strong interaction. Gravitation is usually neglected on subatomic scale, since it is more than 30 times weaker than the three other forces. The spin of field particles is given in units of $\hbar$. Taken from [1].

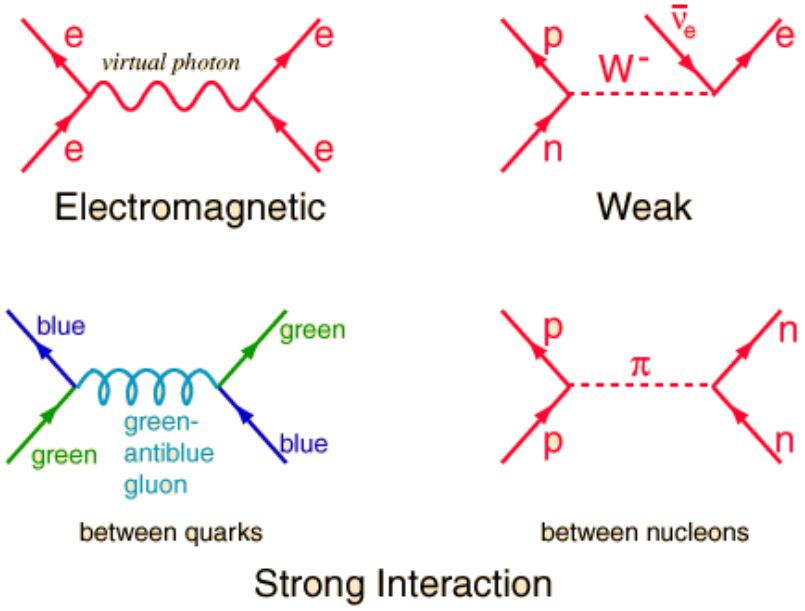

Figure 1.1: Examples of electromagnetic, weak and strong interaction. They represent interaction of two electrons, beta-decay of a neutron, interaction of a blue quark with a green quark and interaction of two nucleons respectively. Taken from Ref. [5].

The mean life-time of every interaction can be determined from Heisenberg' s uncertainty principle

$$\Delta E \Delta t \approx \frac{\hbar}{2}. \tag{1.3}$$

It is then possible to calculate the range of the interaction, since it is proportional to its duration

$$\Delta r = c\Delta t.$$

Interaction is characterised by the square of interchanged momentum $\vec{q}^2$ Real bosons are massless, implying $\vec{q}^2 = 0$. On contrary, in interactions $\vec{q}^2 \neq 0$, which has no physical meaning. Hence the particles interchanged during interactions are necessarily virtual. The conservation laws can be violated during such processes for a time period given by (1.3).

1.3 Parity and charge conjugation

Parity operation characterises the transformation of wave function ψ caused by inversion of spatial coordinates $\vec{r} \to -\vec{r}$. Momentum is also changed during such processes as $\vec{p} \to -\vec{p}$, while the angular momentum $\vec{L}$, the spin $\vec{s}$, and the total angular momentum $\vec{J}$ are preserved. The electromagnetic field is transformed as follows: $\vec{A} \to -\vec{A}$ and $\vec{B} \to \vec{B}$. Here $\vec{A}$ stands for magnetic vector potential, $\vec{B}$ denotes magnetic field. The two quantities are linked through the following equation:

$$\vec{A} = \nabla \times \vec{B}. \tag{1.4}$$

The parity operation can be written as

$$\hat{P}\psi(\vec{r}) = \psi(-\vec{r}).$$

Parity is conserved in both strong and electromagnetic interactions, yet it is violated in weak processes. Parity operation over left-handed neutrino would produce a right-handed state. However, such a particle has never been observed. Hence the maximal violation of parity in neutrino interactions.

Strong and electromagnetic interactions are invariant under another operation - charge conjugation. Such operation reverses the sign of the electric charge and magnetic momentum of a particle. In other words, the charge conjugation operation changes a particle into its antiparticle:

$$\hat{C}\,|p\rangle = |\bar{p}\rangle$$

On the other hand, charge conjugation invariance is violated in weak interactions. Analogically to parity operation, a left-handed neutrino subjected to charge conjugation operation would be transformed into a left-handed antineutrino, which again is excluded by the Standard Model.

1.3.1 CP symmetry

The combined operation CP transforms a left-handed neutrino into a right-handed antineutrino. For some time, CP was really thought to be invariant in weak interactions. Nevertheless, it was observed to be violated in decay of neutral kaons [2, 6].

Neutral Kaon Decay

Kaons are the lightest mesons containing a strange quark or antiquark. Neutral kaons are K^0 $(d\bar{s})$ and its antiparticle $\overline{K}^0$ $(s\bar{d})$. However, they do not exist on their own. The particles we actually observe are superpositions of the two states. We do distinguish two varieties according to their life time: K_S^0 (as for *short*), with $\tau_S = 0.089$ ns, and K_L^0 (as for *long*), with $\tau_L = 51.7$ ns. If we

denote K_1^0 and K_2^0 the kaon CP eigenstates, their respective forms would be as follows:

$$K_1^0 = \sqrt{\tfrac{1}{2}}\left(K^0 + \overline{K}^0\right) \quad CP = +1$$

$$K_2^0 = \sqrt{\tfrac{1}{2}}\left(K^0 - \overline{K}^0\right) \quad CP = -1.$$

Since we assume that K_S^0 and K_L^0 are CP eigenstates, we can write

$$\begin{aligned} K_S^0 &= K_1^0 \\ K_L^0 &= K_2^0. \end{aligned} \tag{1.5}$$

The K_S^0 would therefore decay into two pions with CP = +1 while K_L^0 would decay into three pions with CP = -1.

However, small portion of K_L^0 was observed to decay into two pions. Rather than by (1.5) the observed neutral kaons would be represented by

$$\begin{aligned} K_S^0 &= \tfrac{1}{\sqrt{1+|\varepsilon|^2}}(K_1^0 - \varepsilon K_2^0) \\ K_L^0 &= \tfrac{1}{\sqrt{1+|\varepsilon|^2}}(K_1^0 + \varepsilon K_2^0). \end{aligned} \tag{1.6}$$

where $\varepsilon \approx 2.3 \cdot 10^{-3}$ is a parameter describing the magnitude of CP violation.

The above described phenomenon is called *indirect CP violation* and is caused by mixing of the two kaon states K_1^0 and K_2^0 [1]. The mixing itself arise from the oscillation of neutral kaons. This means that mesons from an originally pure K^0 beam will turn into their antimatter counterparts and vice-versa. Examples of such transitions can be found in Fig. 1.2. The figure shows also transitions of D^0 and B^0 mesons. Oscillation is a characteristic feature of neutral mesons.

Another significant feature of K_L^0 can be seen in its leptonic decay modes [2]. First of the modes is $K_L^0 \longrightarrow e^+ + \nu_e + \pi^-$, its rate is denoted as R^+ while the second decay writes as $K_L^0 \longrightarrow e^- + \overline{\nu_e} + \pi^+$, with rate R^-.

The K_L^0 is more likely to decay into a positron since

$$\Delta = \frac{(R^+ - R^-)}{(R^+ + R^-)} = (3.3 \pm 0.1) \cdot 10^{-3}. \tag{1.7}$$

Such a violation, which occurs in the actual decay of neutral kaons, is referred to as *direct CP violation*.

$D^0 - \overline{D}^0$ and $B^0 - \overline{B}^0$ mixing

As we saw in previous text, the K^0 and $\overline{K}^0$ particles can turn one into the other. This quality is known as oscillation and explains the observed mixing of

neutral kaons. Moreover, the $D^0(c\bar{u})$, $B^0(d\bar{b})$ and $B_S^0(s\bar{b})$ mesons are believed to possess the same quality. Transitions of neutral mesons into corresponding antimesons are displayed in Fig. 1.2.

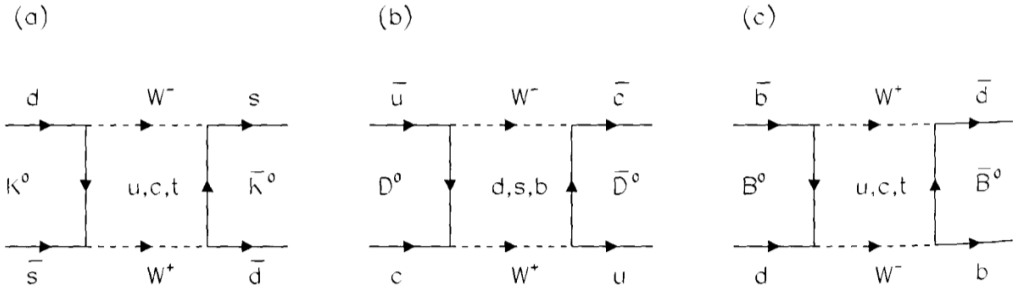

Figure 1.2: Mixing of neutral mesons. Observed mesons are superpositions of the two states - particle and its antiparticle. The two state oscillate – the particle turns into the antiparticle and viceversa. Transitions a) $K^0 \longrightarrow \bar{K}^0$ b) $D^0 \longrightarrow \bar{D}^0$ c) $B^0 \longrightarrow \bar{B}^0$. Taken from Ref. [1].

$B^0 - \overline{B}^0$ mixing was measured with the BABAR detector at the SLAC laboratory and with the Belle device at KEKB, Japan. The measurements indicated mixing in neutral B mesons, thus providing a clear evidence for CP violation in B system [8, 9].

Moreover, mixing of neutral D mesons was reported by Belle [10] and BABAR [11]. The LHCb experiment at CERN also observed evidence for CP violation in the charm sector [13].

Belle investigated the quantities y_{CP}, the deviation from unity of the ratio of effective lifetimes in the decay modes $D^0 \to K^+K^-$ and $D^0 \to K^-\pi^+$

$$y_{CP} = \frac{\tau(D^0 \to K^-\pi^+)}{\tau(D^0 \to K^+K^-)} - 1,$$

and A_Γ, the asymmetry of effective lifetimes measured in decays of D^0 and $\overline{D}^0$ to K^+K^-

$$A_\Gamma = \frac{\tau(\overline{D}^0 \to K^+K^-) - \tau(D^0 \to K^+K^-)}{\tau(\overline{D}^0 \to K^+K^-) + \tau(D^0 \to K^+K^-)}.$$

In other words, y_{CP} and A_Γ give magnitude of the indirect and direct CP violation respectively.

The results are as follows [10]:

$$y_{CP} = (13.1 \pm 3.2_{stat} \pm 2.5_{syst}) \cdot 10^{-3} \tag{1.8}$$

$$A_\Gamma = (0.1 \pm 3.0_{stat} \pm 1.5_{syst}) \cdot 10^{-3}. \tag{1.9}$$

The parameter y_{CP} is different from zero by more than 3σ. The neutral D mesons do mix, the indirect CP violation was truly observed. However, the value of A_Γ is consistent with zero, the direct CP violation was not observed. Similar results were achieved by BaBar [11]:

$$y_{CP} = (11.6 \pm 2.2 \pm 1.8) \cdot 10^{-3}. \tag{1.10}$$

The indirect CP violation was observed. The no-mixing hypothesis was in this case excluded at 4.1σ [11]. The direct CP violation was not measured. No sign of direct CP violation was found in previous measurements [12].

The LHCb gives values of the mixing parameter y_{CP} and A_Γ [13]

$$y_{CP} = (5.5 \pm 6.3_{stat} \pm 4.1_{syst}) \cdot 10^{-3} \tag{1.11}$$

$$A_\Gamma = (-5.9 \pm 5.9_{stat} \pm 2.1_{syst}) \cdot 10^{-3}. \tag{1.12}$$

The value of y_{CP} is consistent with (1.8) and (1.10). The value of A_Γ is consistent with (1.9) and with zero. Note that the value of (1.11) is also consistent with zero. Nevertheless, future updates and new data will precise values of y_{CP} and A_Γ and reduce errors.

As a conclusion, we can say that observation of the indirect CP violation in $D^0 - \overline{D}^0$ system was proved.

CP violation and the Standard Model

Standard Model makes some predictions about the level of direct CP violation [2]. For the quarks, weak and strong eigenstates are not identical. Weak eigenstates are rather mixture of strong eigenstates. The flavour states are transformed into the weak states by the following transformation:

$$\begin{pmatrix} d' \\ c' \\ b' \end{pmatrix} = \begin{pmatrix} V_{ud} & V_{us} & V_{ub} \\ V_{cd} & V_{cs} & V_{cb} \\ V_{td} & V_{ts} & V_{tb} \end{pmatrix} \begin{pmatrix} d \\ c \\ b \end{pmatrix} \tag{1.13}$$

The above matrix is called *CKM matrix* (after its proponents Cabbibo, Kobayashi and Maskawa). Module of each element $|V_{ij}|^2$ gives probability that quark i decays into quark j. Absolute values for V_{ij} in (1.13) are [2]:

$$\begin{vmatrix} V_{ud} & V_{us} & V_{ub} \\ V_{cd} & V_{cs} & V_{cb} \\ V_{td} & V_{ts} & V_{tb} \end{vmatrix} \approx \begin{vmatrix} 0.972 & 0.221 & 0.004 \\ 0.221 & 0.975 & 0.039 \\ 0.008 & 0.038 & 0.999 \end{vmatrix}$$

The CKM matrix V is unitary, hence for the elements in right top corner of V^*V matrix we can write [2]:

$$V_{ud}^* V_{ub} + V_{cd}^* V_{cb} + V_{td}^* V_{tb} = 0.$$

This can be plotted in the complex plane as a *unitarity triangle* as in Fig. 1.3. The three angles of the triangle (denoted α, β and γ) can be determined from decays of neutral B-mesons. Objective of these measurements is to find out whether the observed CP violation is consistent with predictions of the Standard Model.

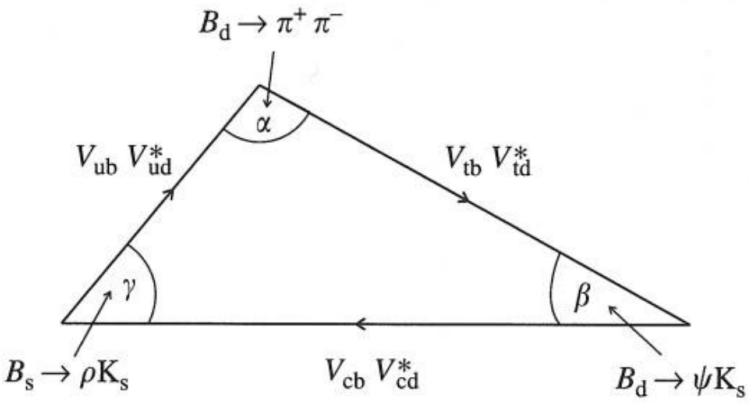

Figure 1.3: Unitarity triangle from CKM matrix. Each element V_{ij} determine probability of quark transition $i \longrightarrow j$. Values of the three angles can be derived from decays of neutral B-mesons. Taken from Ref. [2].

1.3.2 CPT theorem

Both CP and T violation were observed [2]. However, once combined, the resulting CPT operation should be an exact symmetry. The CPT theorem predicts such a symmetry. As a result, particles and antiparticles would have exactly the same mass, spin and lifetime. Their magnetic moment and charge would be of the same value, yet of different sign. Therefore it should be also possible to combine antiparticles and form bound states in the same way as with particles.

1.4 Parton model

It was known for some time that hadrons are not point-like particles, but are of finite size. It was only natural to expect they would have some internal structure [1]. Study of deep inelastic scattering (DIS) of electrons on protons showed that hadrons are indeed constituted of so called *partons*, later identified as quarks and gluons. Moreover, partons are point-like and therefore truly elementary as was demonstrated by DIS at higher energies.

As was demonstrated in Section 1.2, electromagnetic interaction ep takes place via exchange of virtual photon of value of momentum transfer squared $Q^2 = |\vec{q}^2|$. Q^2 is inversely proportional to the wavelength of the interchanged photon [1]. At sufficiently high Q^2 (therefore at high energies), the photon has wavelength short enough to interact rather with composing particle than with the proton as a whole. The spin of interacting partons was determined as $1/2\hbar$, they were identified as quarks.

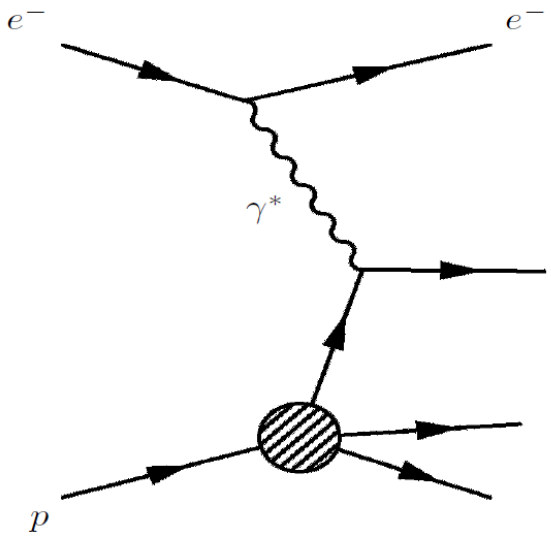

Figure 1.4: Deep inelastic scattering of an electron on a proton. Taken from Ref. [14].

The exact number of quarks in proton was yet to be determined. Proton composition *uud* provides a satisfactory explanation of its quantum numbers. Such quarks are called *valence quarks*. Nevertheless, nucleon could also contain a non-specified number of *sea quarks*, more precisely a quark-antiquark pairs. Its quantum numbers would remain unchanged. Existence of sea quarks was also proved experimentally [1].

Still, gluons were yet to be discovered. It is only natural to expect that the total momentum shared by quarks should be equal to the momentum of proton. However, only about a half is carried by quarks - the other half seems to have mysteriously vanished. Therefore the missing portion of momentum have to be bore by particles that cannot be detected in electromagnetic and weak interactions. These particles were identified as gluons.

Gluons are electric-neutral, which means they cannot be directly measured in deep inelastic scattering. On the other hand, they bear colour charge both in form of colour and anti-colour and can thus interact with each other. The colour charge increases with distance, while at short distances it has much smaller impact. Partons then seem to be free particles with small coupling constant, this quality being known as asymptotic freedom. As the coupling constant grows with distance between particles, at certain distance the force becomes too strong and quarks can move no further. The partons are thus confined within hadrons.

1.5 Antiparticles

To every particle, there is a corresponding antiparticle - an antimatter counterpart of identical mass and lifetime yet of opposite charge and other additive quantum numbers. When a particle collides with its antimatter doppleganger, they both annihilate. However, they do not really disappear, since the total energy and momentum of the system (the particle-antiparticle pair) must be conserved. Thus the pair is transformed into other particles and their respective antiparticles.

The idea of antimatter was first proposed by Paul Dirac. He noticed that the wave equation describing an electron had four possible solutions. Yet only two of them actually described the electron. The other two solutions were attributed to the so-called antiparticle of exactly the same properties but of opposite charge.

In quantum mechanics, the stream of electrons of energy E and momentum $\vec{p}$ can be represented by following wave function:

$$\psi = A\ e^{-i(Et-\vec{p}\cdot\vec{x})/\hbar}. \tag{1.14}$$

From the relativistic term

$$E^2 = p^2c^2 + m^2c^4 \tag{1.15}$$

the energy can be principally of both positive and negative value which means (1.14) might as well represent stream of particles of negative energy $-E$ and momentum $-\vec{p}$ not only in the opposite direction $-\vec{x}$ but also backwards in time. Hence the term $Et - \vec{p}\cdot\vec{x}$ becomes $(-E)(-t) - (-\vec{p})\cdot(-\vec{x})$ and the two terms equal.

Negatively charged electrons with $E < 0$ streaming backwards in time are equivalent to a flow of positively charged electrons moving forwards, their energy being positive. The negative energy state thus corresponds to an antiparticle, positron, with $E > 0$. Such an antiparticle was really discovered shortly after Dirac postulated its existence.

Dirac's equation was originally written to explain the behaviour of an electron. Since electron is a fermion, one can easily conclude that other fermions would also obey this rule. Thus to every fermion, there should be an antifermion. Furthermore, one should expect the existence of antiproton and antineutron, whose existence was proved experimentally (further details are given in Chapter 2). Few examples of particles and their antiparticles can be found in Table 1.4.

1.6 Matter - antimatter asymmetry

All the visible Universe is most likely built uniquely of matter. Even though several theories assume that amount of matter and antimatter are even, no observation supporting this idea have so far been reported.

Quarks and leptons			
particle	charge	antiparticle	charge
electron	-1	positron	$+1$
e-neutrino	0	e-antineutrino	0
up-quark	$+2/3$	up-antiquark	$-2/3$
down-quark	$-1/3$	down-antiquark	$+1/3$
strange-quark	$-1/3$	strange-antiquark	$+1/3$
Hadrons			
particle	quark content	antiparticle	quark content
proton	uud	antiproton	$\bar{u}\bar{u}\bar{d}$
neutron	udd	antineutron	$\bar{u}\bar{d}\bar{d}$
Λ	uds	$\bar{\Lambda}$	$\bar{u}\bar{d}\bar{s}$
K^0	$d\bar{s}$	$\bar{K}^0$	$s\bar{d}$
π^+	$d\bar{u}$	π^-	$u\bar{d}$
π^0	$(u\bar{u} - d\bar{d})/\sqrt{2}$	$\bar{\pi}^0$	$(u\bar{u} - d\bar{d})/\sqrt{2}$

Table 1.4: Examples of particle-antiparticle pairs. Fermions are listed in the upper part (with respective charges). The bottom part shows hadrons together with their quark contents [4].

However, we assume that equal amount of matter and antimatter were created after the Big Bang. But then all the matter should have annihilated long ago. Indeed, there are evidences that shortly after the Big Bang, a huge amounts of particles and antiparticles had vanished in what we call the Great Annihilation, yet had there been a small surplus of matter, it would have survived. Processes causing the baryon and lepton number violation had to take place shortly after the Big Bang.

Several conditions had to be fulfilled to create baryon-antibaryon asymmetry we observe [2]. These are known as *Sakharov criteria*. The three conditions are:

- baryon number violating interactions,
- non-equilibrum situation,
- CP and C violation.

The first condition is obvious, assuming there were originally the same number of baryons and antibaryons. However, there is still no direct evidence for these reactions. As for the second criterion: in equilibrum, any reaction destroying baryon number is counterbalanced by a reaction that creates it. The third requirement serves to distinguish unambiguously between matter and antimatter, as pointed out in Section 1.3.1.

There are various theories trying to explain the observed predominance of matter over antimatter. One of the most likely models suggests that such an asymmetry might have arisen from decay of massive Majorana neutrinos [2, 7].

1.6.1 Massive Neutrinos

Neutrino is a neutral lepton of very small mass, $m_\nu \sim 0.1$ GeV/c^2. Neutrino exists only in left-handed form while antineutrion is always right-handed (see 1.1.2).

However, the above classification assumes neutrinos are so-called Dirac particles. This means particle and antiparticle are quite distinct (e.g. quark-antiquark). Since the only observed difference between neutrino and antineutrino is their handedness, we can as well consider them as two forms of one particle. Particles that are at once their own antiparticles are called Majorana particles.

Existence of massive neutrinos might provide an explanation to the fact that the ordinary neutrino is so light. Its mass would be suppressed by the mass of the heavy neutrino [2].

Massive neutrinos could have existed shortly after the Big Bang and could have died out due to the decay into light neutrinos:

$$N \longrightarrow H + \nu \tag{1.16}$$

where N and ν denotes massive and ordinary neutrino respectively and H represents a Higgs boson emitted during the decay.

There is no reason to assume that massive neutrinos would have decayed into neutrinos and antineutrinos equally. They could have preferred one form to the other. Such a disbalance between leptons and antileptons could provoke an asymmetry between quarks and antiquarks through simultaneous interactions. These would produce new quarks or antiquarks, their numbers being uneven.

Chapter 2

Discovering antimatter

During the 20^{th} century, announcements of observations of new particles were the order of the day. The following text reviews discoveries of positron, antiproton, antineutron and of antihydrogen atom.

2.1 Positron

The positron was discovered by C. D. Anderson in 1932, just shortly after its theoretical prediction [15]. This was undoubtedly a big event at that time, since the original idea of antimatter used to be mainly considered as a theoretical tool created to explain the seemingly paradoxical electron state with negative energy.

The first positrons were actually observed much earlier by D. Skobeltzyn in 1923 [7]. He sought for evidence of gamma rays in cosmic rays, using a cloud chamber situated in uniform magnetic field. Each particle could be thus identified according to the curvature of its track, and from the total energy-loss. The radius of the track depends on the charge of the particle q, its velocity v (and therefore its energy) and on the magnitude of applied magnetic field B:

$$R = \frac{qv}{mB}$$

Skobeltzyn noticed that some of the particles seemed to turn the wrong way. However, no explanation was found at time.

During the measurements carried by Anderson, both positive and negative particles occurred in likewise abundances, most of them bearing a unit electric charge. The negatively charged particles were interpreted as electrons. However, the positively charged particles could not be protons, as was first suggested, as their tracks at measured energies would be much shorter. Furthermore, these particles exerted the same specific ionisation as electrons.

To see whether the track was induced by an electron, with negative charge, moving downwards or a positive particle of the same mass as the electron, moving upwards, a lead plate was installed in the chamber. Particles would suffer

from a greater energy-loss when crossing the plate. Therefore the corresponding part of the track would be more curved. This is illustrated in Fig. 2.1, showing a positron moving upwards.

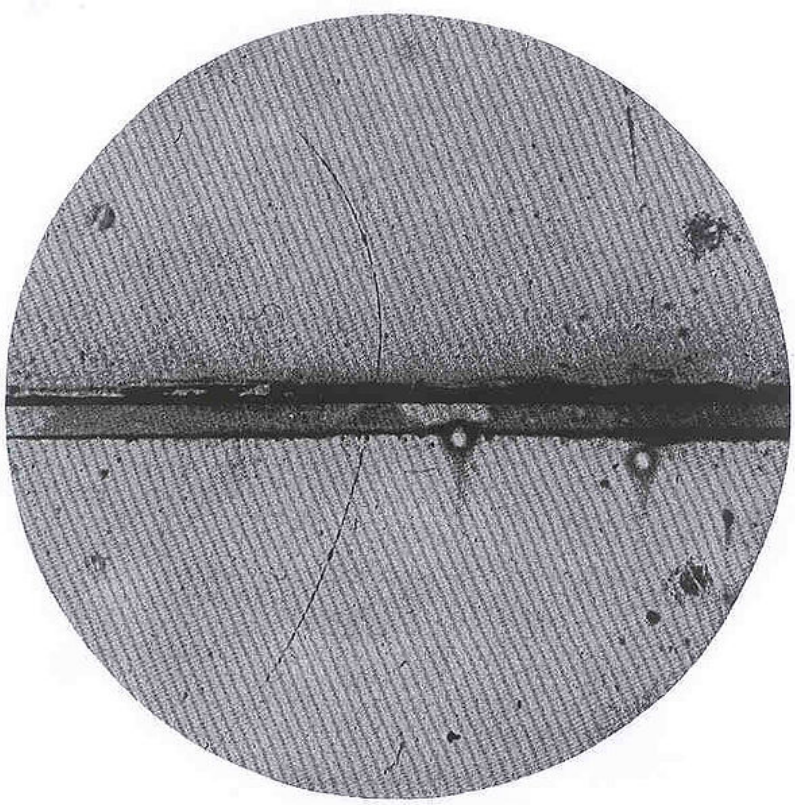

Figure 2.1: Positron, moving upwards, crossing a lead plate. The track is bent more significantly in the upper part of the chamber (upper part of the picture), since the particle lost a great portion of energy while crossing the lead plate. Magnetic field points into the paper. Taken from Ref. [15].

2.2 Antiproton

Once the positron was discovered, scientists started to inquire whether other elementary particles, such as proton, have their antimatter doppelgangers. Eventually, the antiproton was discovered in 1955 by O. Chamberlain [16].

The measurements were carried at the Bevatron facility at Berkeley National Laboratory. Actually, one of the main purposes of Bevatron was to investigate existence of antiproton.

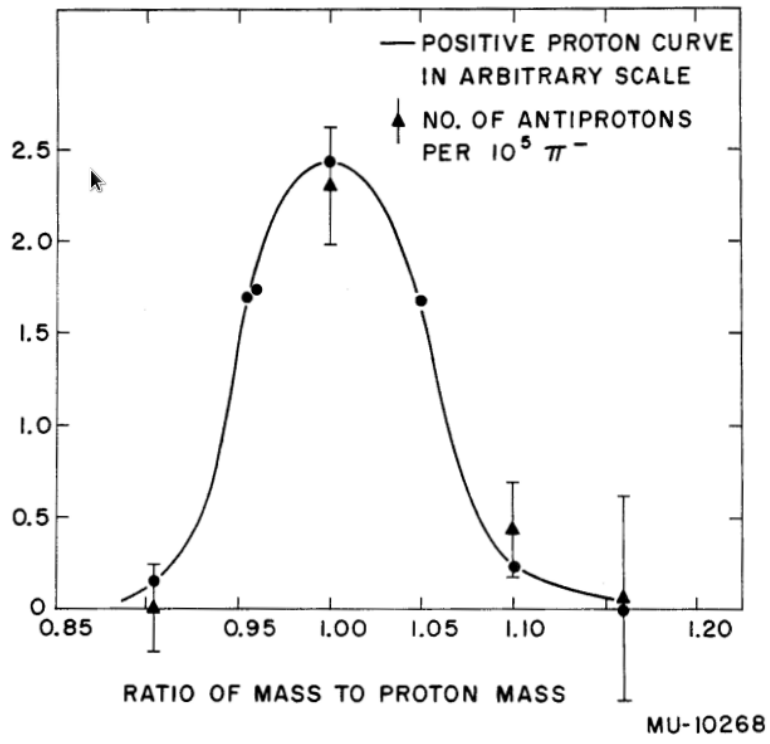

Figure 2.2: Number of particles versus ratio of mass to proton mass. The solid curve represents the mass resolution of the apparatus as obtained with protons. Taken from Ref. [16].

In the original article [16], detection of 60 antiprotons was reported. Proton beam hitting the Cu target produced secondary particles. Negative ones were separated and deflected into a separate beam. Their masses were determined from their momenta and velocities. A peak of negative particles around the proper mass for proton was observed (see Fig. 2.2). Furthermore, no particles were known at time to have sufficiently long lifetime to get from the place of collision to the counters (time-of-flight about 10^{-8} s).

Observation of negatively charged hydrogen ions was excluded - by the time the ions would get to the counters, they would have been already stripped of their electrons [16].

2.3 Antineutron

The first antiproton was also observed at the Bevatron facility. The first report was written by B. Cork and others in 1956. The main interest of studying antineutron was that the charge conjugation has less visible impact on neutral particles [17].

The aim of the experiment was to detect events of annihilation of antineutrons. These were produced from antiprotons, by charge-exchange. Protons of energy of 6.2 GeV were let to collide with beryllium target. With a system of deflecting magnets, a 1.4 GeV/c beam of negative particles was obtained. Antiprotons were distinguished from negative mesons by comparison of their times of flight. Set of six scintillators was used to detect the particles along the line. The antiproton beam was then shot to a thick converter X, see Fig. 2.3. Products of the interaction passed through the pair of scintillators (S_1 and S_2) and subsequently to the Čerenkov counter C. Antineutrons would not interact with the scintillators, however, they would provoke a large pulse of light in the Čerenkov counter.

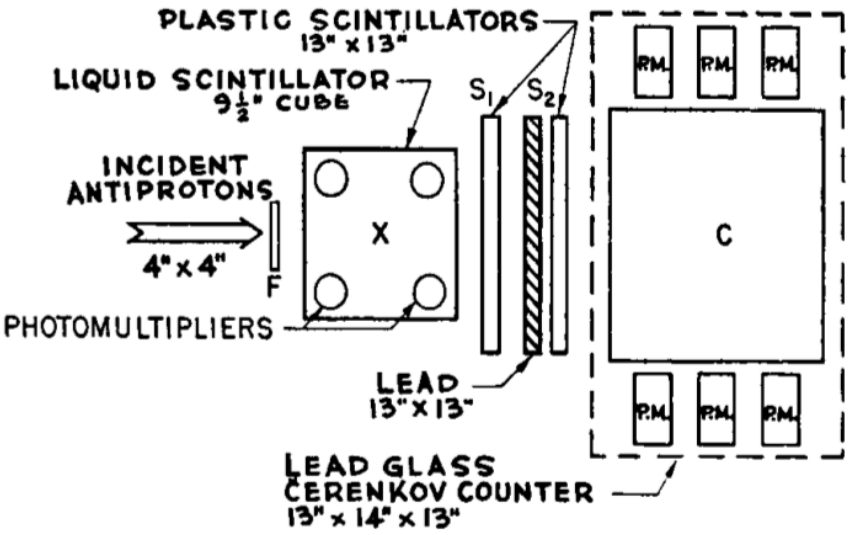

Figure 2.3: Antineutron detecting system. X is the charge converter, S_1 and S_2 are scintillation counters, C is a lead-glass Čerenkov counter. Antiproton beam hits into X. Antiprotons are either converted into antineutrons or annihilate with nucleons in the converter. Neutral particles produced from such a reaction continue to C, where they provoke signal. Antineutrons, originating in charge-exchange, would provoke Čerenkov light in C. Yet corresponding impulse in X would be much weaker compared to impulse from annihilation of protons. Taken from Ref. [17].

Both high-energy gamma rays and neutral particles such as mesons or neutrons could have been misinterpreted as antineutrons. To prevent so, a thick lead plate was installed between the two scintillators. To distinguish antineutrons from other neutral events observed by counter C, the charge converter was made of scintillating solution. Neutral events could be thus separated from those originating in an annihilation of antiproton, which would be indicated by a large pulse in X. The less violent process of charge-exchange would be indicated by a significantly weaker pulse.

2.4 Antihydrogen

The very first detection of antihydrogen was done at the Low Energy Antiproton Ring in CERN (LEAR) by the PS210 experiment. Production of 11 antihydrogen atoms was reported in 1995 [18].

There are two possible variants of producing antihydrogen - either in flight or at rest. The PS210 choose the in-flight option.

An antiproton and a positron were brought close together both in momentum space and energy. While passing a nucleus with charge Z, antiproton will interact with its Coulomb field and produce e^+e^- pair. The positron is then captured by the antiproton. Fast moving antihydrogen is produced this way. The two-photon mechanism of lepton-pair production was estimated:

$$\bar{p}Z \longrightarrow \bar{p}\gamma\gamma Z \longrightarrow \bar{p}e^+e^-Z \longrightarrow \overline{\mathrm{H}}e^-Z \tag{2.1}$$

A schematic view of mechanism (2.1) is shown in Fig. 2.4.

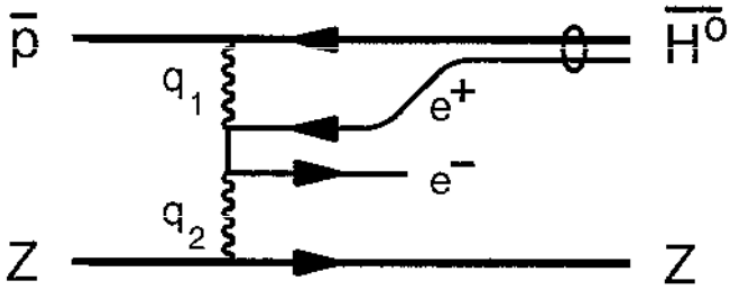

Figure 2.4: A schematic view of the two-photon mechanism for e^+e^- and $\bar{\mathrm{H}}$ production at LEAR. The antiproton passing nearby nucleus of charge Z. The two particles interact through Coulomb interaction, thus producing e^+e^- pair. The positron is subsequently captured by antiproton. Taken from Ref. [18].

Once the neutral atom was formed, it exited the ring. The $\bar{\mathrm{H}}$ was stripped into the silicon counter in the LEAR vacuum system. Positron was detected through annihilation into two back-to-back photons, each of energy 511 keV. The antiproton detection was somewhat less straightforward. The energy loss $\mathrm{d}E/\mathrm{d}x$ of the antiproton was measured by series of three silicon counters. The antiproton then passed through a set of scintillator detectors. Deflection of charged particles was also registered - observed events were compared to the expected deflection for $\bar{p}$ from antihydrogen.

Chapter 3

Hypernuclei

Hyperons are baryons containing at least one strange quark. They can interact with nucleons within nuclei and result in a new, exotic form of matter – hypernuclei.

The interest of studying hypernuclei lies in the possibility of expanding our knowledge into an exotic region. The strangeness gives new dimension to the chart of nuclides, such a chart can be found in Fig. 3.1. Hyperons have a short lifetime – of order of 10^{-10} s. This means that the path they travel is about the order of $c\tau \approx 10$ cm after which they decay weakly. Hypernuclei serve as a "femto-laboratories" to investigate YN and YY interaction. Direct measurement of YN and YY cross-sections is far too difficult due to the very short lifetime of hyperons. In general, YN and YY interactions are weaker than NN.

Three-body interactions are also allowed. Actually, the ΛNN three-body interaction is essential tool for investigation of the structure of the Λ-hypernuclei [19].

3.1 The Λ Hyperon

The very first hyperon ever observed was the hyperon Λ in 1952 by M. Danysz and J. Pniewski. During investigation of cosmic rays at 26 km above ground with a meteorological balloon carrying a photographic emulsion, they observed collision of an energetic proton with a nucleon in the emulsion. All the particles produced during the collision stopped soon, leaving a short track in the emulsion. One of them, however, decayed into two lighter particles. The observed event is shown in Fig. 3.2. The characteristic decay pattern is called V^0 *decay* (the name was derived from its shape).

The characteristics of the Λ are as follows: its mass being $m(\Lambda) = 1115.684 \pm 0.006$ MeV/c^2, strangeness quantum number $S = -1$ and lifetime $\tau = 263 \pm 2$ ps [4].

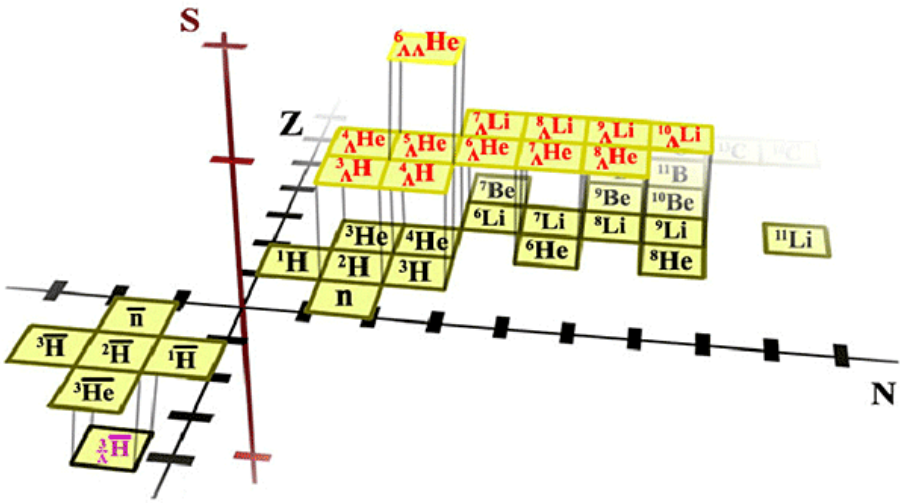

Figure 3.1: A nuclide chart extended into the strangeness sector. Normal nuclei lie in the (N, Z) plane. The negative sector of the chart is occupied with antinuclei. Hypernuclei lie in the octant above the positive part of the plane (N, Z). Antihypernuclei lie in the octant below the negative part of the (N, Z) plane. Taken from Ref. [41].

A list of hyperons can be found in Table. 3.1.

	m [MeV/c^2]	S	I	J^P [$\hbar$]	τ [ps]
$\Lambda^0(uds)$	1115.683 ± 0.006	-1	0	$1/2^+$	263.1 ± 2.0
$\Sigma^+(uus)$	1189.37 ± 0.07	-1	1	$1/2^+$	80.18 ± 0.26
$\Sigma^0(uds)$	1192.642 ± 0.024	-1	1	$1/2^+$	$(7.4 \pm 0.7) \times 10^{-11}$
$\Sigma^-(dds)$	1197.449 ± 0.030	-1	1	$1/2^+$	147.9 ± 0.011
$\Xi^0(uss)$	1314.86 ± 0.20	-2	1/2	$1/2^+$	0.29 ± 0.009
$\Xi^-(dss)$	1321.71 ± 0.07	-2	1/2	$1/2^+$	0.1639 ± 0.0015
$\Omega^-(sss)$	1672.45 ± 0.29	-3	0	$3/2^+$	0.0821 ± 0.0011

Table 3.1: List of hyperons [4].

3.1.1 Structure of Λ-hypernuclei

The ${}^{A}_{\Lambda}Z$ nuclei is composed of Z protons, $(A-Z-1)$ nucleons and of one Λ. In its ground states, all the nucleons are spread as in the ground state of ${}^{(A-1)}Z$, while the Λ is in the lowest energy state. Since the hyperon is distinguishable from the nucleons (it carries strange quantum number), it is not subjected to

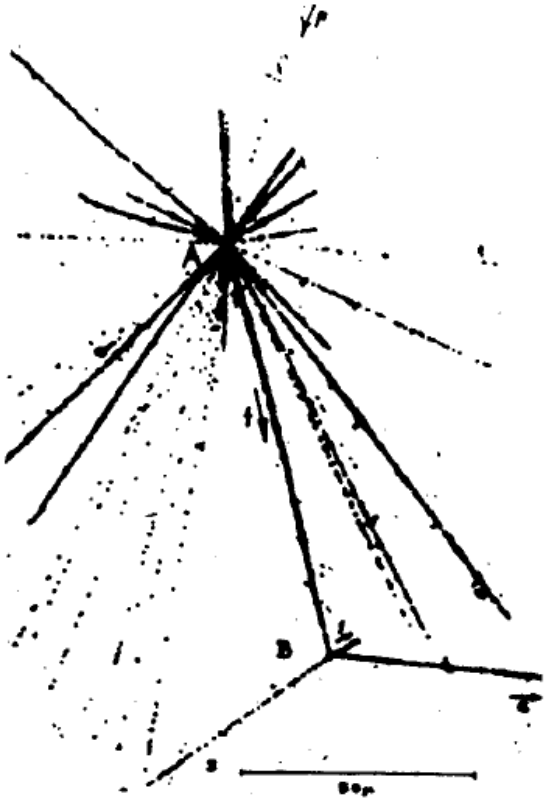

Figure 3.2: The first observed decay of a hypernucleus. The decay was produced by a cosmic ray particle (track p, direction of the track is indicated by the arrow) interacting with a nucleus in the emulsion located at A. The ejected hypernucleus (indicated by track f) decayed at B. Taken from Ref. [20].

the Pauli exclusion principle. Hence it can occupy all quantum states already filled with the nucleons. An example of structure of ^{12}C hypernucleus can be found in Fig. 3.3. A neutron from the p-shell changed into a Λ hyperon. The Λ would occupy the lowest free energy state. If there is more than one hyperon in the nucleus, the hyperons have to obey the exclusion principle [19].

As was mentioned at the beginning of the chapter, the ΛNN interaction is essential for further study of the structure of the Λ-hypernuclei, such as hypertriton ${}^{3}_{\Lambda}$H. The hypertriton is the lightest hypernuclei, it is a weakly bound state formed of $(pn\Lambda)$. The Λ binding energy is [19]

$$B_\Lambda({}^{3}_{\Lambda}\mathrm{H}) \equiv c^2[M({}^{3}_{\Lambda}\mathrm{H}) - M({}^{2}\mathrm{H}) - m(\Lambda)] \simeq -130 \text{ keV}. \tag{3.1}$$

Both neutron and Λ are unstable in free space and decay through weak channels [19]. The energy released in free decay of the neutron is $Q_n^{free} \simeq$

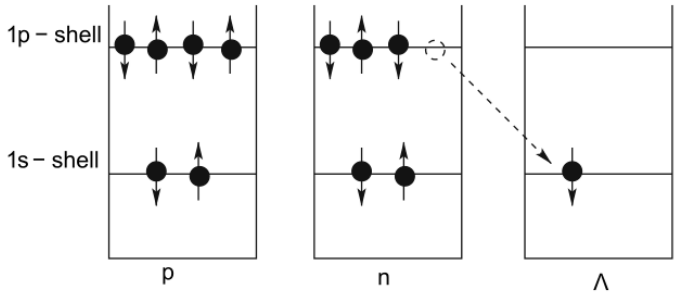

Figure 3.3: A simple model for the ^{12}C hypernucleus. The figure shows a transition which changes a neutron into a Λ. The nucleus remains in its ground state. The structures of nucleons in single shells are independent. States with lowest energies are occupied as first. Taken from Ref. [21].

0.72 MeV, while the binding energy of the neutron in the nucleus is $B_n \simeq -8$ MeV. Hence the neutron bound in a nucleus is generally stable. On the other hand, the energy released by Λ decay is $Q_\Lambda^{free} \simeq 40$ MeV. Its binding energy in a nucleus is $|B_\Lambda| \lesssim 27$ MeV, which means the hyperon is unstable even when bound in a nuclear system.

3.2 Observation of ${}^{6}_{\Lambda}$H hypernucleus at DAFNE

DAFNE (sometimes written as DAΦNE) stands for Double Annihilation ring for Nice Experiments. It is a electron-positron collider located at the INFN[1] Frascati National Laboratory, Italy. DAFNE started its operation in 1999. The accelerator consists of two circular rings, one for electrons and one for positrons, which overlap at two intersection points. Energy of each beam is set to 510 MeV. The unstable $\phi(1020)$[2] particle is produced, which decays into neutral and charged K mesons [22]. DAFNE aims to study CP and CPT symmetries in neutral kaon systems, however, the charged kaons K^- can be used to produce hypernuclei.

The FINUDA (Fisica Nucleare a DAFNE) detector studies the spectra and non-mesonic decays of Λ-hypernuclei. The hypernuclei are produced via bombarding a thin target by K^- beam. Recently, FINUDA claimed having observed the neutron-rich ${}^{6}_{\Lambda}$H hypernucleus [23]. The ${}^{6}_{\Lambda}$H nuclei are produced in following reaction:

$$K^- +^6 Li \longrightarrow^6_\Lambda \mathrm{H} + \pi^+. \tag{3.2}$$

[1] Istituto Nazionale di Fisica Nucleare

[2] Quark content of ϕ mesons is $c_1(u\bar{u} + d\bar{d}) + c_2(s\bar{s})$, from [4].

The hypernucleus then decays through the channel

$$ {}^{6}_{\Lambda}\mathrm{H} \longrightarrow {}^{6}\mathrm{He} + \pi^{-}. \tag{3.3} $$

The data collected during the period of 2003 – 2007 were analysed. To reduce background, coincidence of pions π^+ from (3.2) with π^- from (3.3) was required.

Both production and decay occur at rest since the ${}^{6}_{\Lambda}\mathrm{H}$ stops in the target in a time shorter than its lifetime [23]. Single events are characterised by their total kinetic energy $T_{sum} \equiv T(\pi^+) + T(\pi^-)$:

$$ T_{sum} = [M(K^-) + M(p) - M(n) - 2M(\pi)]c^2 - B({}^{6}\mathrm{Li}) + B({}^{6}\mathrm{He}) - T({}^{6}\mathrm{H}) - T({}^{6}_{\Lambda}\mathrm{H}) \tag{3.4} $$

where M denote corresponding masses, B denote binding energies and T stands for kinetic energies. Both $T({}^{6}_{\Lambda}\mathrm{H})$ and $T({}^{6}\mathrm{H})$ depend on binding energy $B_{\Lambda}({}^{6}_{\Lambda}\mathrm{H})$.

FINUDA collaboration focused on events with $T_{sum} = 203 \pm 1$ MeV and with pion momenta of $p_{\pi^+} \approx 250$ MeV/c and $p_{\pi^-} \approx 130$ MeV/c. Distribution of raw total kinetic energy for $\pi^{\pm}$ coincidence events is shown in Fig. 3.4 while Fig. 3.5 gives momenta of detected pions.

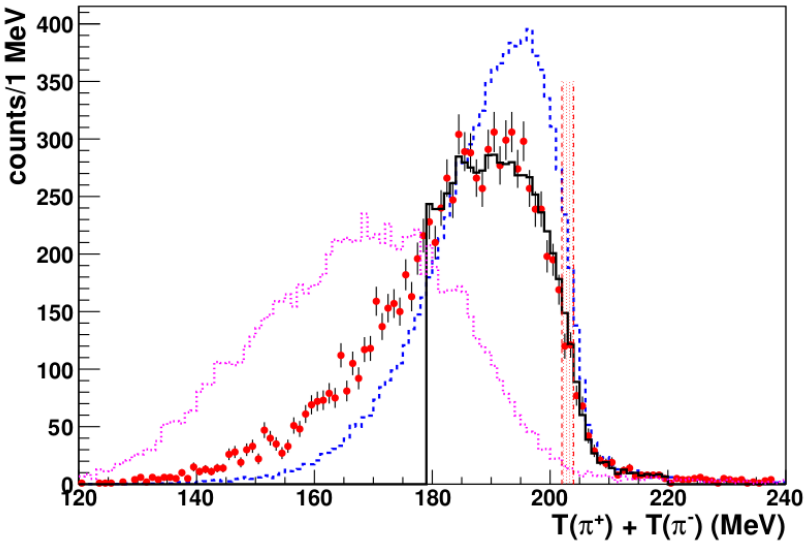

Figure 3.4: Distribution of raw total kinetic energy T_{sum} for $\pi^{\pm}$ coincidence events. Red dots represent measured data. The vertical red bars represent the cut $T_{sum} = 202 - 204$ MeV. Blue and violet histograms originate from of background simulations. Taken from Ref. [23].

In total three ${}^{6}_{\Lambda}\mathrm{H}$ candidates were observed [23]. The candidates are listed in Table 3.2 together with values of mass derived from production (3.2) and from their decay (3.3). The mean value for the ${}^{6}_{\Lambda}\mathrm{H}$ mass is

$$ m({}^{6}_{\Lambda}\mathrm{H}) = 5801.4 \pm 1.1 \text{ MeV}/c^2. \tag{3.5} $$

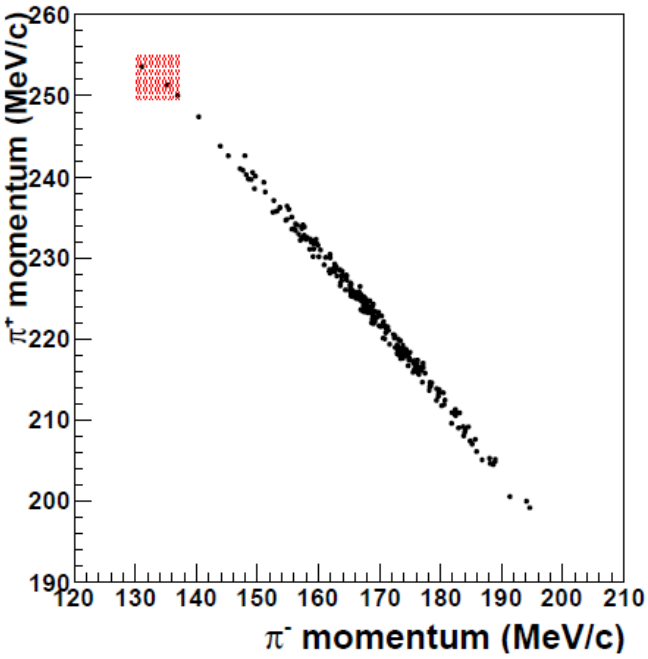

Figure 3.5: π^+ momentum vs π^- momentum for events with $t_{sum} = 202 - 204$ MeV. Red square highlights events with $p_{\pi^+} = 250 - 255$ MeV/c and with $p_{\pi^-} = 130 - 137$ MeV/c. Taken from Ref. [23].

The values of the mass associated with the ${}^{6}_{\Lambda}$H production are slightly higher than those associated with its decay. However, the difference between the two values is within 1σ for all three candidates.

T_{summ} [MeV]	p_{π^+} [MeV/c]	p_{π^-} [MeV/c]	$m({}^{6}_{\Lambda}\mathrm{H})_{prod}$ [MeV/c^2]	$m({}^{6}_{\Lambda}\mathrm{H})_{prod}$ [MeV/c^2]
202.6 ± 1.3	251.3 ± 1.1	135.1 ± 1.2	5802.33 ± 0.96	5801.41 ± 0.84
202.7 ± 1.3	250.1 ± 1.1	136.9 ± 1.2	5803.45 ± 0.96	5802.73 ± 0.84
202.1 ± 1.3	253.8 ± 1.1	131.2 ± 1.2	5799.97 ± 0.96	5798.66 ± 0.84

Table 3.2: Values of summed kinetic energy $T_{summ} = T(\pi^+) + T(\pi^-)$, momenta p_{π^+} and p_{π^-} and of mass for the three ${}^{6}_{\Lambda}$H candidates from production and from decay respectively. Taken from Ref. [23].

Chapter 4

Antihydrogen

All nature' s laws should be the same under the combined operation of charge conjugation, parity and time reversal - the CPT operation. Thus any experiment carried on antihydrogen should give exactly the same results as for hydrogen.

So far, experiments with positronium and specially prepared helium atoms, which had one electron replaced by an antiproton, showed no signs of violation of CPT symmetry. The antihydrogen would be therefore the first pure antimatter system to be probed.

The very first antihydrogen produced in an experiment was recorded in 1995 at the Low Energy Antiproton Ring (LEAR) at CERN (for more details, please see Section 2.4). The first study reported 11 antihydrogen atoms of relativistic energies [18]. Low energy antihydrogen was first observed only in 2002 at ATHENA and ATRAP devices at Antiproton Decelerator at CERN, which was installed in place of LEAR. Research group working at ALPHA, ATHENA's very successor, recently announced having probed antihydrogen spectrum [32].

4.1 Antiproton Decelerator

Antiproton Decelerator (AD) started its operation in 2000. It replaced the previous device used to decelerate antiprotons, LEAR, which had to be closed down in order to free resources for LHC. A schema of the AD ring is shown in Fig. 4.1.

Antiprotons are obtained through collisions of protons of energy of 26 GeV with a fixed iridium target [28]. Some of the antiprotons are collected and sent into the AD ring, where they are cooled through stochastic and electron cooling to 5.3 MeV [29].

The stochastic cooling reduces transverse momenta of individual particles in a bunch. Fluctuations (i. e. particles moving away from the bunch) are detected and corrected. The correction is usually done by a device called 'kicker', which 'kicks' the bunch. The particles thus loose a part of their energy - they are 'cooled'. The electron cooling is done by letting the particles to interact with

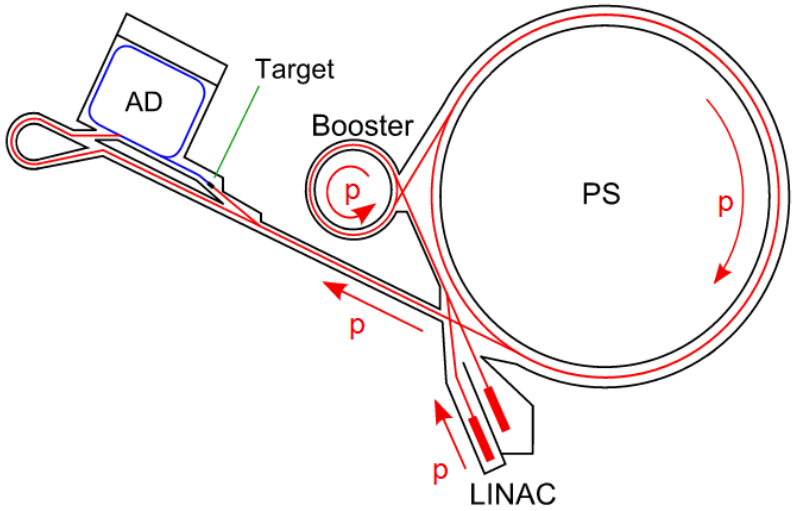

Figure 4.1: Schematic view of the Proton Synchrotron and of the Antiproton Decelerator at CERN. Taken from Ref. [26].

cold (low-energy) electrons.

The current experiments installed at the AD ring are ALPHA, ATHENA, ATRAP, ASACUSA, ACE and AE$\bar{g}$IS. ATHENA, ALPHA' s predecessor, completed its programme in 2004.

4.2 Trapping of charged and neutral particles

First we will discuss the production of antihydrogen. The formation of antihydrogen takes place in a device called Penning-Malmberg trap. However, the modification of the trap at AE$\bar{g}$IS is different to the one used by ALPHA. General description of the Penning-Malmberg trap can be found in the text bellow.

The Penning-Malmberg trap is a device used to confine charged particles. A schema of such a trap is shown in Fig 4.2. The trap consists of a solenoidal magnet, which creates a uniform magnetic field, and of a series of hollow cylindrical electrodes, creating spatially inhomogeneous electric field. The magnetic field confines the particles radially while the electric field confines them axially.

However, once the positrons and antiprotons are mixed, the resulting antihydrogen atoms are neutral. Since they have no charge, they cannot be confined the same way. Nevertheless, neutral particles can be confined through interaction of a magnetic field B with their magnetic moment μ. According to the sign of the magnetic moment, atoms can be either attracted to regions, where

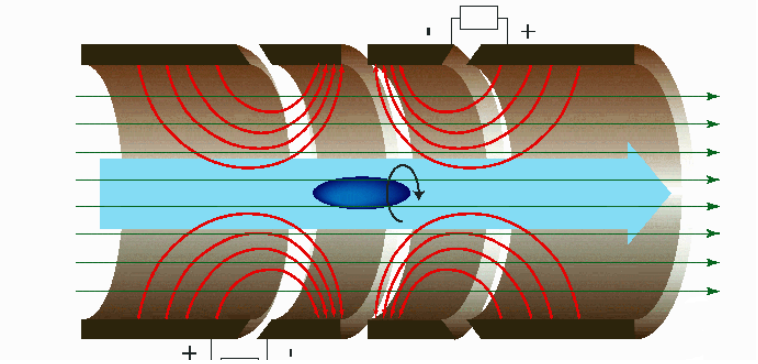

Figure 4.2: A schema of a Penning-Malmberg trap. The solenoidal magnet creates a uniform magnetic field. The electric field created by the electrodes has a saddle point in the centre. Taken from Ref. [27].

B has its maximum ("high-field seeking atoms" with $\mu > 0$), or to regions with minimal B ("low-field seeking atoms" with $\mu < 0$). Half of the antihydrogen atoms will have their spin oriented parallel to the field ($\mu > 0$, these atoms will be lost). The other half will have an antiparallel orientation ($\mu < 0$), these atoms will get trapped [24].

In order to trap the atom through interaction of its magnetic dipole moment, magnet of higher order has to be used, i. e. quadrupole or octupole (although the higher the order, the weaker is the field at the centre of the trap). Magnets of order higher than octupole are too weak at the centre of the trap. The confinement is not significant until the atoms move far away from the trap axis. On the other hand, the quadrupole magnet creates an elliptically shaped plasma, which is very unstable [25]. The octupole magnet seems to be the most efficient one. Compared to quadrupole magnet of the same trap depth, the octupole field not only is conveniently low at the centre [31], but it also greatly reduces perturbations on charged plasma[25].

4.3 Probing of antihydrogen spectrum at ALPHA

4.3.1 Antihydrogen production and detection

Trapping of antiprotons and positrons

Antiprotons provided by AD are cooled to the energy of 5.3 MeV. However, such energetic antiprotons cannot be used for antihydrogen formation. Additional deceleration is therefore required [29]. The antiprotons are let to pass through a foil called degrader. Huge portion of collected antiprotons annihilates with nucleons in foil. However, this process is very cheap and the number of surviving

antiparticles is sufficient. The particles are slowed down to few keV and are trapped in a Penning-Malmberg trap, pictured in Fig. 4.3a.

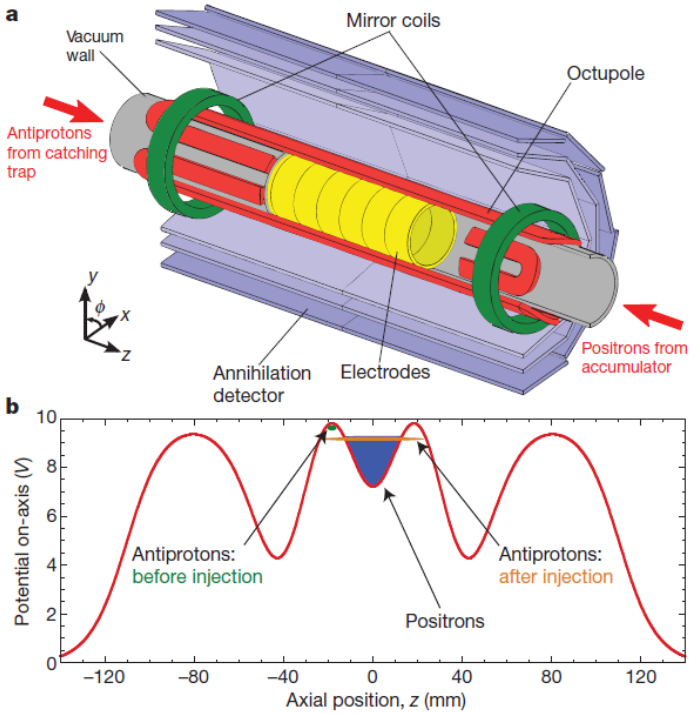

Figure 4.3: (a)The annihilation detector and Penning-Malmberg trap installed at the ALPHA device. The electrodes create a spatially inhomogeneous field which confines the charged particles axially. The solenoidal magnet produce a homogeneous magnetic field that confines the charged particles radially. Once formed, the neutral particles are confined by the magnetic field created by solenoid and the mirror-coils. The drawing is not to scale. (b) Merging of positrons and antiprotons in nested Penning trap. The z coordinate is measured with respect to the centre of the trap. Taken from Ref. [30].

The trap used by ALPHA consists of a superconducting octupole magnet and two axially separated short solenoid mirror-coils, which create strong uniform magnetic field and of series of hollow cylindrical electrodes, creating an electric field. The trapping field created by the mirror coils can be seen in Fig. 4.4. The trapping area is surrounded by a three-layer silicon detector. As the magnetic field is generated by superconducting magnets, enabling a brief shutdown (with reaction time of 9 ms [31]) necessary for successful antihydrogen detection, the apparatus has to be cooled to 4.2 K with liquid helium.

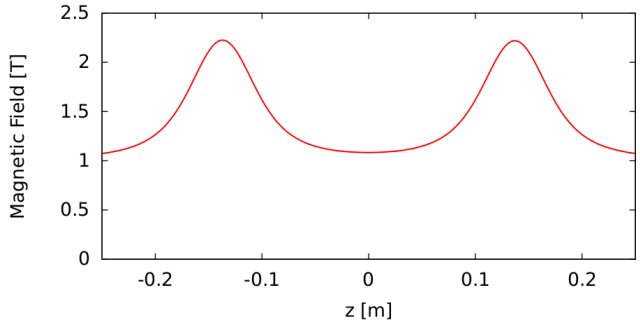

Figure 4.4: Magnetic field inside of a Penning-Malmberg trap. Neutral atoms are confined at the centre. Taken from Ref. [30].

Antiprotons are injected into the trap, which has been pre-filled with electrons. As a consequence, antiprotons are indirectly cooled by interactions with electrons, which are in equilibrum with the cryogenically cooled trap. Cooled antiprotons can be thus stored or used for experiments. Positrons are gained from a radioactive source ^{22}Na [29].

Antihydrogen formation

Antiprotons and positrons are injected into the Penning-Malmberg trap (see Fig. 4.3b). The two species are placed into their respective potential wells [30]. The antiprotons are excited into the positron plasma by an oscillating electric field. The two clouds are merged at the lowest possible relative velocity. Positrons and antiprotons are let to interact for the period of 1 s. After that, all remaining charged particles are disposed of. To ensure no antiprotons will get "mirror-trapped" by the magnetic gradients, four pulses of "clearing" axial electric field of up to 500 Vm^{-1} are applied [31]. The first measurements of antihydrogen annihilation proved no charged particles remained in the trap after the clearing pulses [30]. These measurements were recorded with three variations of clearing electric field. The three variations are: left bias, when any remaining antiprotons would be deflected into the left side of the apparatus at the trap shutdown; right bias with antiprotons deflected to the right side of the trap and no-bias. During the no-bias measurements, all electrodes are at ground and no deflection occurs. Distribution of released antihydrogen atoms and antiprotons is shown in Fig. 4.5. Fig 4.5a compares measured annihilation to data from numerical simulation of antihydrogen behaviour and annihilation after the shutdown. Fig. 4.5b compares measured data to predictions for mirror-trapped antiprotons, data were simulated for all three variations of clearing field.

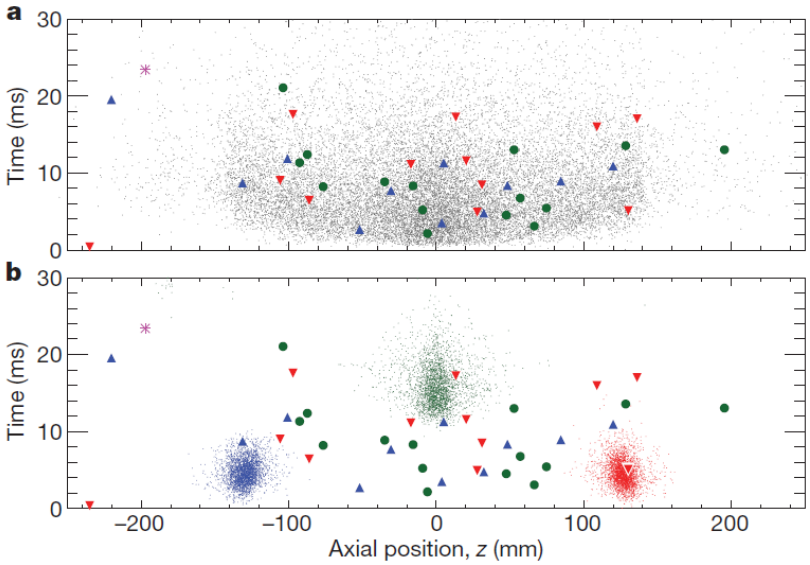

Figure 4.5: Distribution of released antihydrogen and antiprotons. (a) Measured $t-z$ distribution for annihilation obtained with three variations of clearing electric field: left bias (blue triangles), when antiprotons trapped would be deflected to the left, right bias (red triangles), when any remaining antiprotons would be deflected to right and no bias (green circles), when all electrodes are at ground during the shut-down of the trap, thus no deflection occurs. The grey dots are from numerical simulation of antihydrogen released during shutdown. (b) Experimental $t-z$ distribution, as above, shown along with results of numerical simulations of mirror-trapped antiprotons released from trap. Again green dots for no-bias, blue dots for left bias and red dots for right bias. Taken from Ref. [30].

Detection of antihydrogen

The detection of antihydrogen is very straightforward [29]. The antihydrogen atoms are released from the trap and let to collide with the detector. ALPHA looks for events with corresponding annihilation detected.

The antiprotons can interact with both protons and neutrons in the matter. Such reaction generally results with production of several charged pions. These are detected by a three layer silicon detector – track of each pion can be thus reconstructed. The vertex lies on the intersection of detected tracks. Positrons, on the other hand, will annihilate with the electrons in the detector. Two back-to-back photons, each with energy of 511 keV, are usually released.

Hence ALPHA searches for events with two photons of the right energy on a line passing through the antiproton annihilation vertex. An example of such

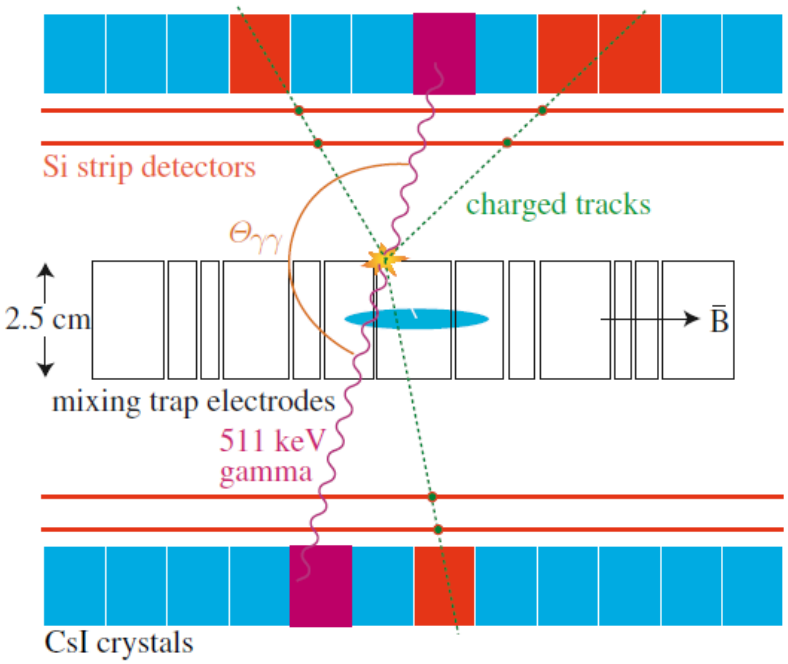

Figure 4.6: Detection of antihydrogen annihilation in ATHENA. The $\bar{H}$ atom annihilates with the matter of the trap. The antiproton can annihilate both with protons and neutrons, such an interaction produces several charged pions. These are registered by the three-layer silicon detector, position of the annihilation vertex is determined from intersection of their tracks. Annihilation of positron with electron from the magnet results in production of two back-to-back photons, each of 511 keV. Both annihilation events has to be time-coincident and originate in the same place. Taken from Ref. [29].

an event is shown in Fig. 4.6.

Events time-correlated with trap shutdown (release of antihydrogen) are observed in case of successful trapping. The maximal recorded confinement time was 2000 s with $\sigma = 2.5$, the 1000 s time was measured with significance $\sigma = 8.0$ [31]. Summary of time measurements is listed in Table 4.1. Sufficiently long confinement time is crucial to carry further experiments on antihydrogen, necessary time to perform planned microwave transitions is of order ~ 100 s.

Avents with annihilation of antimatter from cosmic rays can also be recorded. However, these can be easily recognised from their track topologies which are much different from those caused by antihydrogen. The tracks of cosmic rays are very energetic and pass straight through the detector. Track topologies for both types of event are shown in Fig. 4.7

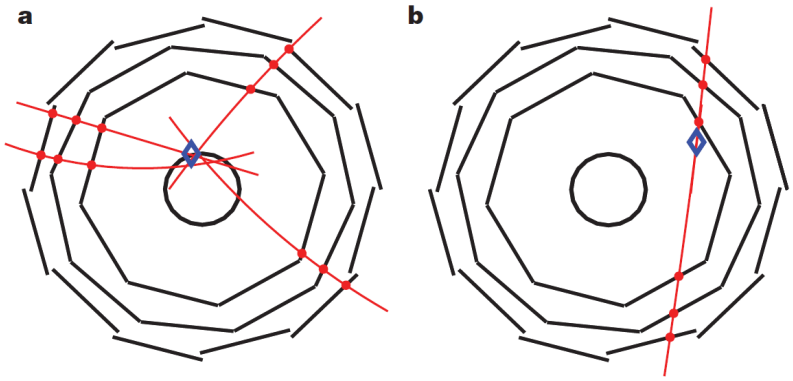

Figure 4.7: Track topology of (a) antiproton annihilation and (b) cosmic rays. Taken from Ref. [30].

Confinement time (s)	0.4	10.4	50.4	180	600	1000	2000
Number of attempts	119	6	13	32	12	16	3
Detected events	76	6	4	14	4	7	1
Estimated background	0.17	0.01	0.02	0.05	0.02	0.02	0.004
Statistical significance	$\gg$20	8.0	5.7	11.0	5.8	8.0	2.6

Table 4.1: Summary of antihydrogen time confinement measurement by ALPHA. Antihydrogen atoms were detected by characteristic annihilation after the trap shutdown. Taken from Ref. [31].

4.3.2 Probing the antihydrogen spectrum

ALPHA plans to measure resonant quantum transitions of the $\bar{\mathrm{H}}$ electron induced by microwaves of given frequency f [32]. In presence of magnetic field, the energy levels of the electrons in the atom are split into two sub-levels with different projections of the spin (see Fig. 4.8). The two possible energy states are separated by energy

$$\Delta E = |\mu| B \tag{4.1}$$

where μ is the magnetic dipole moment of the $\bar{\mathrm{H}}$ atom and B is magnitude of the used magnetic field. To excite the atom from the state with lower energy to the state with higher energy, we need to apply electromagnetic radiation of the right frequency f, obeying

$$hf = \Delta E = |\mu| B. \tag{4.2}$$

The trapped antihydrogen is proved to be in its ground state [31]. However, once it is excited, it is no longer trapped. Hence the atom escapes from the

centre of the trap, hits the wall of the magnet and annihilates. The annihilation process was described in previous section.

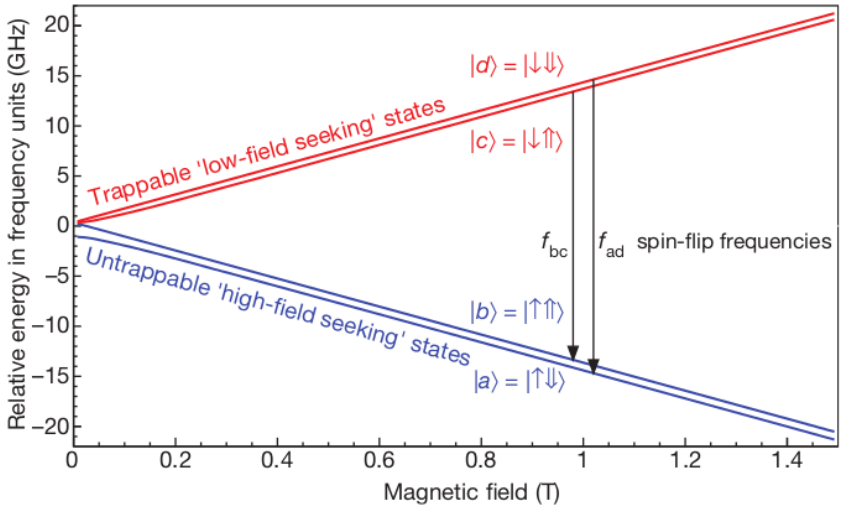

Figure 4.8: The relative hyperfine energy levels of the ground states of the hydrogen (antihydrogen) atom in presence of magnetic field. The possible transitions are $|c\rangle \to |b\rangle$ and $|d\rangle \to |a\rangle$. The single arrow indicates the electron (positron) spin of each state vector, the double arrow represents the proton (antiproton) spin. Taken from Ref. [32].

ALPHA investigates transition of antihydrogen from the ground state (1s) to its first excited state (2s) [32]. The 2s state is very long-lived (with lifetime $\tau = 122$ ms [29]). Hence the energy between the two states is well-defined (from (1.3)). Only microwaves of the right energy (4.2) can induce such transition. In case of different energy of microwaves, all trapped atoms should remain in the trap until the shutdown.

All together six series of measurements were recorded [32]. Series 1 measured the on-resonance mode for some minimum value of magnetic field B^A and resonant microwave field of frequency f^A. For series 2, the minimum of magnetic field was shifted to $B^B > B^A$ (by increasing the current in mirror-coils) while the frequency remained the same. This is called the off-resonance mode. For series 3, the magnetic field was kept at value B^B and the frequency was tuned to f^B so that the microwaves were in resonance again. Configuration for series 4 measurement was somewhat similar to the one in series 2. Two additional series of measurements in no-microwave mode (5 and 6) were carried to cross-check results for on- and off-resonance mode. Apart from changes in the minimal value of the magnetic field and the frequency of applied microwaves,

Mode (series)	Number of attempts	Detected atoms	Trapping rate
on-resonance (1)	79	1	0.01 ± 0.01
off-resonance (2)	88	16	0.18 ± 0.05
on-resonance (3)	24	1	0.04 ± 0.04
off-resonance (4)	22	7	0.32 ± 0.12
no-microwave (5)	52	17	0.33 ± 0.08
no-microwave (6)	48	23	0.48 ± 0.10

Table 4.2: Series summaries for the disappearance mode analysis. The numbers of surviving atoms were counted after the application of the microwaves. Six series of measurements were carried, two for on-resonance mode, two for off-resonance mode and two for no-microwave mode. Taken from Ref. [32].

the experimental procedure was identical for all six series.

Two distinct, complementary type of data were collected - the so called *disappearance* (summed up in Table 4.2) and *appearance mode* (see Fig. 4.9). During the disappearance mode, annihilation were counted after the shutdown in a 30-ms window. Effective trapping rate for each mode could be thus determined. Trapping rate for the on-resonance mode should have been reduced due to escape of confined atoms. The three rates were then compared. The appearance mode data came from monitoring the antihydrogen annihilation throughout the entire time the trap is turned on, events were counted for on-resonance, off-resonance and no-microwave mode.

The off-resonance and no-microwave data in Table 4.2 give approximately the same trapping rate of $\bar{\mathrm{H}}$ atoms. The on-resonance data show that only few percent of trapped $\bar{\mathrm{H}}$ survived. The interpretation is that the trapped atoms were excited by the resonant microwave field, which allowed them to escape.

The number of annihilation events for on-resonance mode in Fig. 4.9 is much greater for the first 30 s than for the time $t = 30 - 180$ s. These annihilation (during the first 30 s) are therefore interpreted as originating from released antihydrogen. The annihilation for off-resonance and no-microwave mode are considered as background.

Thus we can conclude both from Table 4.2 and Fig. 4.9 that projection of the spin of the trapped atom can indeed be reversed by resonant microwave field. The measurement described above is a proof-of-principle experiment. Precise localisation of resonance and the spectral line-shape are to be determined in future [32].

4.4 AE$\bar{\mathrm{g}}$IS

AE$\bar{\mathrm{g}}$IS stands for Antihydrogen Experiment Gravity Interferometry Spectroscopy and represents another experiment studying antimatter at CERN. Its main goal is the direct measurement of the Earth's local gravitational acceleration g on

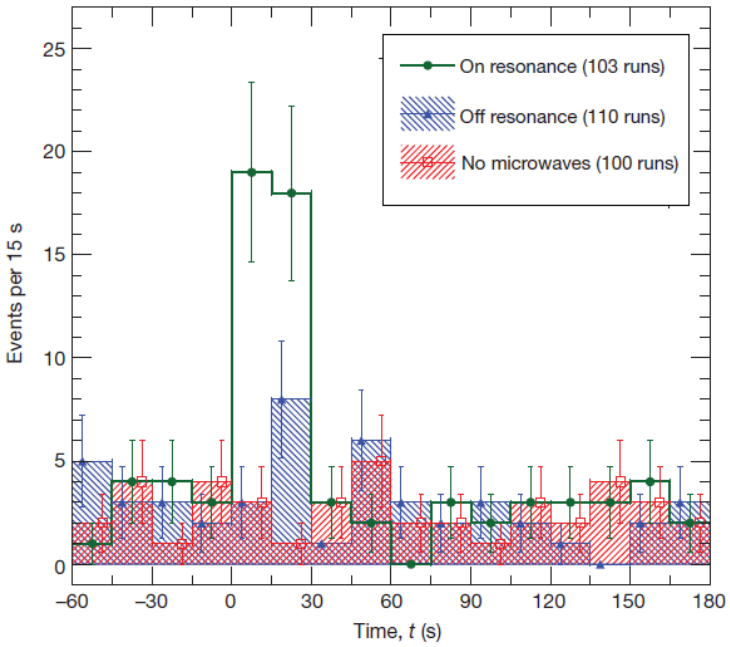

Figure 4.9: The number of appearance mode annihilation as a function of time between the end of antihydrogen production and the trap shutdown. Microwaves are first applied at $t = 0$. The number of annihilating antihydrogen during application of microwaves is much greater for on-resonance mode. This implies that the trapped atoms were excited by microwaves. Taken from Ref. [32].

antihydrogen and how it is different to the effects g has on matter [33].

The antihydrogen is produced according to the following equation:

$$Ps + \bar{p} \longrightarrow \bar{H}^* + e^- \tag{4.3}$$

where Ps denotes highly excited positronium state – such state is referred to as Rydberg state and is significant for its high principal quantum number n. In case of AEgIS, n varies from 25 to 35. The reaction is illustrated in Fig. 4.10. The advantages of this reaction is its large cross-section and the fact that antihydrogen thus created comes in a narrow well-defined band of final states [33].

The mechanism of $\bar{\mathrm{H}}$ production is as follows: laser-excited positronia are sent across a Penning-Malmberg trap region containing antiprotons cooled to ~ 100 mK. Such low temperatures allow formation of antihydrogen atoms with low velocity compared to the velocity they will achieve after acceleration ($v \sim 10^2$ ms^{-1}). $\bar{\mathrm{H}}$ is created at velocities of $25 - 80$ ms^{-1}.

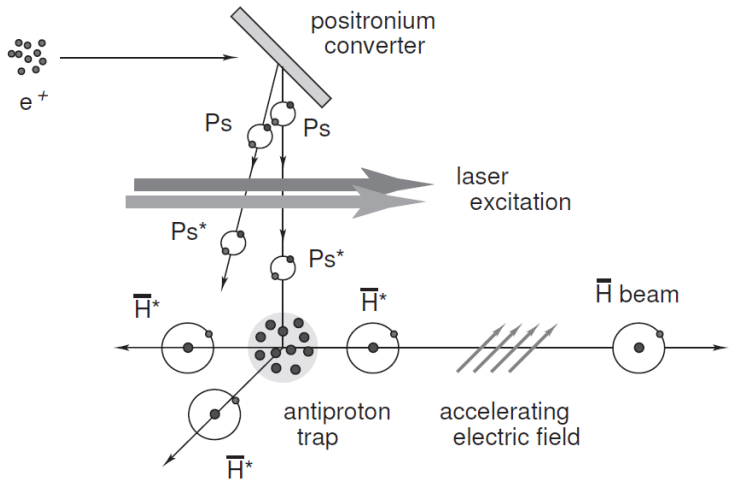

Figure 4.10: Antihydrogen formation and acceleration at AEgIS. Positronia are laser excited to Rydberg state and loaded into a Penning?Malmberg trap. The trap as been pre-filled with cold antiprotons. The two plasmas merge and form $\bar{H}$ atoms. These are no longer trapped and are carried away by the electric field. Taken from Ref. [33].

4.4.1 Measurement of the Antihydrogen Fall

Produced $\bar{H}$ atoms are accelerated by exposing their electric dipole momenta to an electric-field gradient. Rydberg atoms are very sensitive to changes in electric field since their dipole momenta $\sim n^2$ [33]. The $\bar{H}$ is intended to be accelerated to the velocity of about 400 ms^{-1}. The trap does not have to be modified to confine neutral particles as the produced antiatoms will be swept by the electric field, which will prevent their annihilation with the trap.

The beam then travels to a Moiré deflectometer, shown in Fig. 4.12. The deflectometer consists of two identical parallel gratings of the same fringe spacing d,placed at equal distances L, coupled to a position-sensitive detector. The distance between the second grating and the detector is again L. The first two gratings create a shadow pattern, which is displayed onto the third grating. Under the influence of gravity, the beam falls. The shadow pattern is thus vertically displaced by a distance

$$\delta x = -gT^2 = -\frac{gL^2}{v^2} \tag{4.4}$$

where g denotes the Earth's local gravitational acceleration, T and L is the transit time and distance between two consecutive gratings respectively and v is the velocity of the beam. Therefore by measuring δx and T we can determine the value of g for antimatter. As the distance L between the second grating

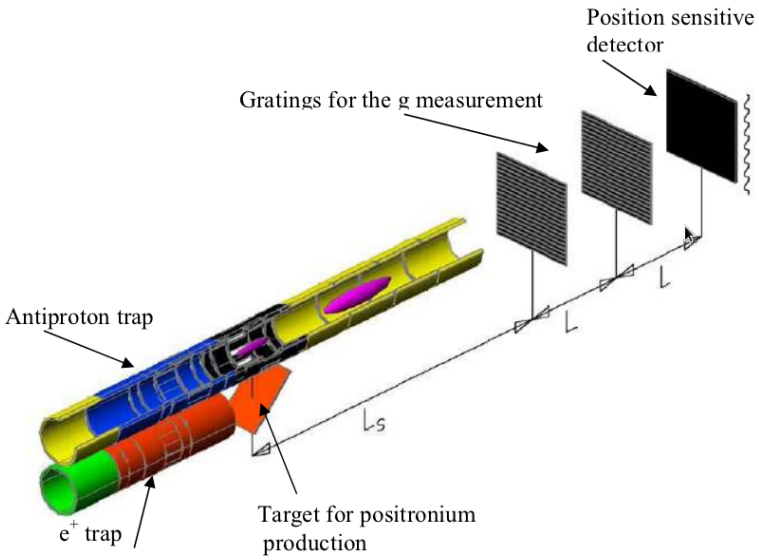

Figure 4.11: Schema of the Penning-Malmberg trap, which serves to merge the antiproton and positron plasma, together with the Moiré deflectometer. The Moiré deflectometer enables the device to measure vertical displacement of the beam. Taken from Ref. [34].

and the detector is constant, the transit time T depends solely on the velocity of the beam v, which can be controlled by the electric field gradient.

The assumed vertical displacement of an antihydrogen beam travelling a distance of $L = 1$ m at the velocity $v \sim 400$ ms^{-1}, subjected to the gravitational field $g \sim 10$ ms^{-2}, is $\delta x = 20\mu m$. However, displacement of single particles due to the divergence of the beam can be up to 10 cm. This problem can be prevented by the use of the Moiré deflectometer, where the first two gratings select propagation direction of the originally divergent beam [35].

The experiment started its operation in spring 2012. Currently, the possibility to produce the antihydrogen atoms is tested. No gravitation measurements are yet scheduled.

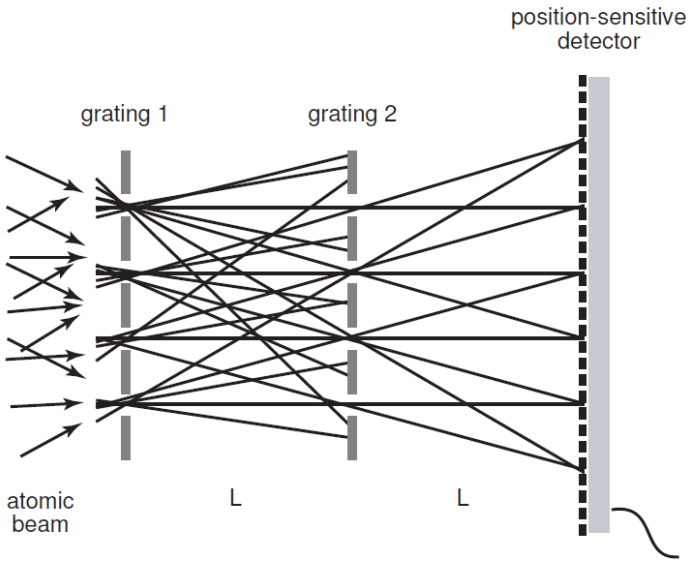

Figure 4.12: Schema of a Moiré deflectometer consisting of two gratings coupled to a position-sensitive detector. The beam, coming from left, is divergent. The gratings select its direction of propagation. The displacement is registered by the position-sensitive detector. Taken from Ref. [33].

Chapter 5

Antinuclei in nucleus-nucleus collisions

High-energy nuclear collisions recreate conditions in the primordial Universe. The hot medium produced during the collisions contains equal numbers of quarks and antiquarks. The relatively short-lived expansion of the hot and dense matter allows the matter to decouple quickly from antimatter, thus preventing annihilation.

In this chapter, we shall focus on observation of antimatter helium-4 nucleus ${}^4\overline{\mathrm{He}}$ and of antihypertriton ${}^3_{\overline{\Lambda}}\overline{\mathrm{H}}$ with the STAR detector at the Relativistic Heavy-Ion Collider.

5.1 The Solenoidal Tracker at RHIC

5.1.1 The Relativistic Heavy-Ion Collider

The Relativistic Heavy-Ion Collider (RHIC), located at the Brookhaven National Laboratory in USA, started its operation in 2000. Its main objective is study of the quark gluon-plasma, the state at which all the matter is believed to have existed few seconds after the Big Bang [36]. In this state, quarks and gluons are no longer confined within nucleons.

The whole complex is shown in Fig. 5.1. The RHIC is an intersection ring with circumference of 3834 m, composed of two independent rings connected through six intersection points where particles collide. The experiments are therefore placed at these points. Currently, there are four experiments installed at RHIC: STAR, PHENIX, BRAHMS and PHOBOS. However, BRAHMS and PHOBOS had already completed their program. The RHIC performs both proton-proton and ion-ion collisions. Heavy- ions (d+Au, Cu+Cu, Au+Au, Cu+Au, U+U) are collided at centre-of-mass energies up to 200 GeV per nucleon-nucleon pair while the maximum centre-of-mass energy for proton-proton collisions is $\sqrt{s_{NN}} = 500$ GeV. The fact that the two rings are inde-

pendent enables the RHIC to collide quite easily asymmetric systems such as d+Au or Cu+Au.

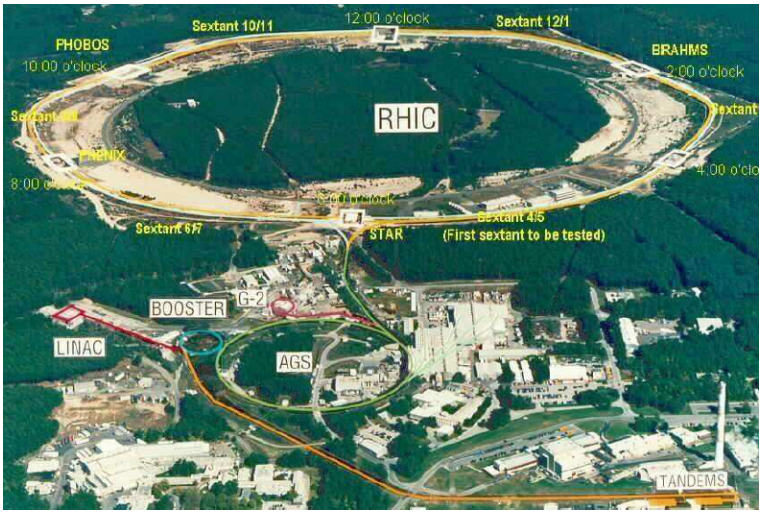

Figure 5.1: Schema of the RHIC accelerator complex. Taken from Ref. [36].

5.1.2 The STAR

The main physics goal of The Solenoidal Tracker at RHIC (STAR) is study of physical effects which occur under extreme conditions, namely production of quark gluon plasma [36, 37]. However, it is also able to study antinuclei [40, 41]. Undoubtedly the most important feature of the STAR is its full azimuthal coverage. Study of the azimuthal particle correlation is therefore possible. The coverage of rapidity is $|\eta| < 1.8$.

The Time Projection Chamber

The primary tracking device is the Time Projection Chamber (TPC). The TPC records tracks of produced particles, measures their momenta and their ionisation energy loss $\mathrm{d}E/\mathrm{d}x$ to identify the particles. TPC has the ability to measure wide range of particle momenta - from 100 MeV/c to over 30 GeV/c. Particles are identified up to 1 GeV/c.

The TPC is a cylindrical unit surrounding the beam-pipe (please see Fig. 5.2, the TPC itself is depicted in Fig. 5.3). The outer diameter is 4 m, the inner is 1 m. It has 4.2 m in length and is divided into two parts by a thin conductive Central Membrane (CM). The detector is seated in a large solenoidal magnet that operates at 0.5 T. The inner electric field is ≈ 135 V/cm. The CM is operated at 28 kV while the read-out caps are at ground. The volume is filled with a P10 gas (90 % argon, 10 % methane) regulated at 2 mbar above

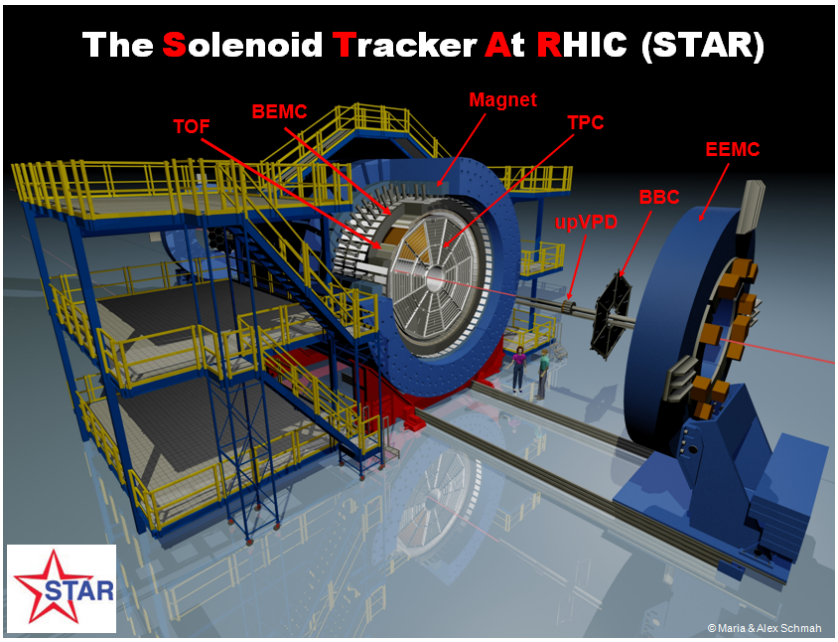

Figure 5.2: Schematic view of the STAR detector.

atmospheric pressure. The P10 gas has remarkably fast drift velocity which peaks at low electric field. The reason to operate at the peak of the velocity is that in such case the drift velocity remains stable even when subjected to small variations in temperature and pressure. Some of the basic parameters of the TPC are listed in Table. 5.1.

While passing the chamber filled with gas, particles ionise the gas. The ionisation produces secondary electrons. These then drift to the read-out caps. The read-out caps are split into 12 sectors. Each sector constitutes of several pad planes. The x and y coordinates of the track are reconstructed from the pad signal of drifting electrons hitting the cap. The z coordinate is calculated from the drift time of the electron cluster, travelling from its origin to the caps, combined with the average drift velocity.

The ionisation energy loss $\mathrm{d}E/\mathrm{d}x$ is given by the Bethe-Bloch formula

$$\frac{\mathrm{d}E}{\mathrm{d}x} = \frac{4\pi n_e z^2 e^4}{m_e \beta^2 c^2} \frac{1}{\beta^2} \left[ln \left(\frac{2 m_e c^2 \beta^2}{I(1-\beta^2)} \right) - \beta^2 \right] \tag{5.1}$$

where m_e is the electron mass, z is the atomic number of the target, β is the velocity of the incident electron, I is the mean excitation potential, n_e is the electron density in the target. Note that the energy loss per unit length is independent of the mass of the particle. Hence the velocity of the particle can be calculated without previous identification of the particle, e. i. without knowing

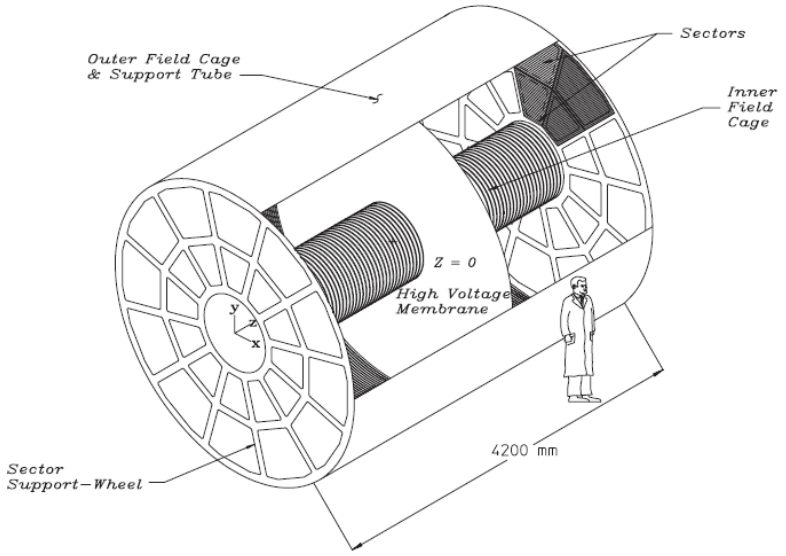

Figure 5.3: Schema of the TPC at STAR. Taken from Ref. [37].

its mass. However, momenta are used to identify particles rather than their velocities. A typical plot of $\mathrm{d}E/\mathrm{d}x$ versus momentum is shown in Fig. 5.4. The black curves show expected values of $\langle \mathrm{d}E/\mathrm{d}x \rangle$ calculated from (5.1) for each particle. Coloured points give energy-loss distribution for given momentum. Data for protons, kaons and pions are plotted. Protons can be clearly identified for momenta up to 1 GeV/c. Pions and kaons cannot be distinguished one from another for momenta greater than 0.7 GeV/c.

The momentum can be found from cyclotron equation

$$p = qBR \tag{5.2}$$

where p is the momentum of the particle with charge q, B is the magnitude of external magnetic field and R is the radius of particle' s curvature. The uniform magnetic field within the TPC is $|B| < 0.5$ T The charge is assumed to be $q = \pm 1e$.

The Time of Flight

The capability of STAR to identify particles can be enhanced by combined use of the TPC and of the ToF. The ToF measures particles velocity β. When used together with particle' s momentum p from TPC, both pieces of information serve to calculate particle' s mass m as

$$m = p\sqrt{1/\beta^2 - 1} \tag{5.3}$$

Length of the TPC	420 cm
Outer Diameter of the Drift Volume	400 cm
Inner Diameter of the Drift Volume	100 cm
Distance: Cathode to Ground Plane	209.3 cm
Cathode Diameter	400 cm
Cathode Potential	28 kV
Drift Gas	90% Argon + 10% methane
Pressure	2 mbar above atmospheric
Drift Velocity	5.45 cm/μs
Signal to Noise Ratio	20 : 1
Magnetic Field	$\pm$ 0.5 T

Table 5.1: Basic parameters of the STAR TPC. Taken from Ref. [37].

The ToF measures start times and stop times of the tracks. The velocity β is found by dividing the particle's path length from the event vertex to the ToF, s, by the time necessary to traverse this path length Δt

$$\beta = \frac{s}{c\Delta t} \tag{5.4}$$

5.2 Observation of antinuclei in high-energy nuclear collisions

5.2.1 Antimatter Helium-4

The $^4\overline{\mathrm{He}}$ consists of two antiprotons and of two antineutrons. So far, it is the heaviest antinucleus ever observed. The STAR detected 18 $^4\overline{\mathrm{He}}$ in Au-Au collisions of centre-of-mass energy of 200 GeV and 62 GeV [40].

Figure 5.5 represents energy loss per track $\langle \mathrm{d}E/\mathrm{d}x \rangle$ versus the magnitude of magnetic rigidity $p/|Z|$. The black curves show expected values for each particle. Only data for $^3\overline{\mathrm{He}}$ (^{3}He) and $^4\overline{\mathrm{He}}$ (^{4}He) are included. In the left part of the figure, four $^4\overline{\mathrm{He}}$ particle are distinctly visible in the area of $p/|Z| < 1.4$ GeV/c. On the right side, the bands of particles centering around the expected values indicate the detector is well-calibrated.

Figure 5.6 shows $\langle \mathrm{d}E/\mathrm{d}x \rangle$ versus mass of the particle $m = p/c\sqrt{t^2c^2/L^2 - 1}$, where t and L are the time of flight and path length respectively and c denotes the speed of light. The ionisation energy is given in $n_{\sigma_{\mathrm{d}E/\mathrm{d}x}}$, multiples of the standard deviation $\sigma_{\mathrm{d}E/\mathrm{d}x}$. In the second panel, a cluster of particles can be seen around the values of $n_{\sigma_{dE/dx}} = 0$ and $m = 3.73$ GeV/c^2, which is the proper mass for ^{4}He. Similar cluster is displayed in the first panel for $^4\overline{\mathrm{He}}$. The bottom panel shows mass distributions for measured data. There is a visible separation

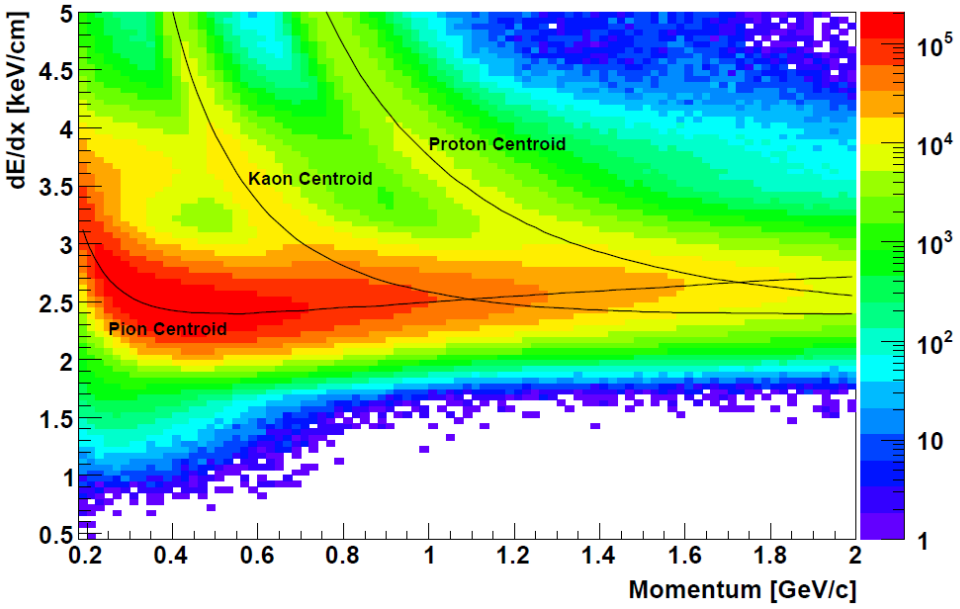

Figure 5.4: A typical plot of $d\mathrm{E}/d\mathrm{x}$ versus momentum from data from TPC. The black curves show expected values of $\langle \mathrm{d}E/\mathrm{d}x \rangle$ for each particle. Coloured points give energy-loss distribution for given momentum. Data for protons, kaons and pions are plotted. Particles can be identified for momenta up to 1 GeV/c. Taken from Ref. [36].

between $^3\overline{\mathrm{He}}$ and $^4\overline{\mathrm{He}}$ peaks, which means one can be clearly distinguished from the other.

The antimatter yield is calculated from the observed counts and compared to the theoretical predictions. Various uncertainties can be avoided through calculation of yield ratios of $^4\mathrm{He}/^3\mathrm{He}$ and $^4\overline{\mathrm{He}}/^3\overline{\mathrm{He}}$, their values being

$$\begin{aligned} {}^4\mathrm{He}/{}^3\mathrm{He} &= (3.0 \pm 1.3_{stat} \pm 0.5_{sys}) \cdot 10^{-3} \\ {}^4\overline{\mathrm{He}}/{}^3\overline{\mathrm{He}} &= (3.2 \pm 2.3_{stat} \pm 0.7_{sys}) \cdot 10^{-3} \end{aligned} \tag{5.5}$$

for central Au-Au collisions at $\sqrt{s_{NN}} = 200$ GeV, which is consistent with theoretical expectations ($^4\overline{\mathrm{He}}/^3\overline{\mathrm{He}} = 2.4 \cdot 10^{-3}$ and $^4\mathrm{He}/^3\mathrm{He} = 3.1 \cdot 10^{-3}$).

The differential yield for $^4\overline{\mathrm{He}}$ ($^4\mathrm{He}$) is then obtained by multiplying the $^4\overline{\mathrm{He}}/^3\overline{\mathrm{He}}$ ($^4\mathrm{He}/^3\mathrm{He}$) ratio with $^3\overline{\mathrm{He}}$ ($^3\mathrm{He}$) yield. Invariant yields as a function of baryon number are displayed in Figure 5.7. The production rate reduces by a factor of $(1.6 \pm 1.0) \cdot 10^3$ for each antinucleon added to the antinucleus, and by a factor of $(1.1 \pm 0.3) \cdot 10^3$ for each nucleon added to the nucleus. In other words, the rate of antinucleus (nucleus) production in high-energy collisions decreases by about factor 1000 with every single antinucleon (nucleon) added. Antinuclei

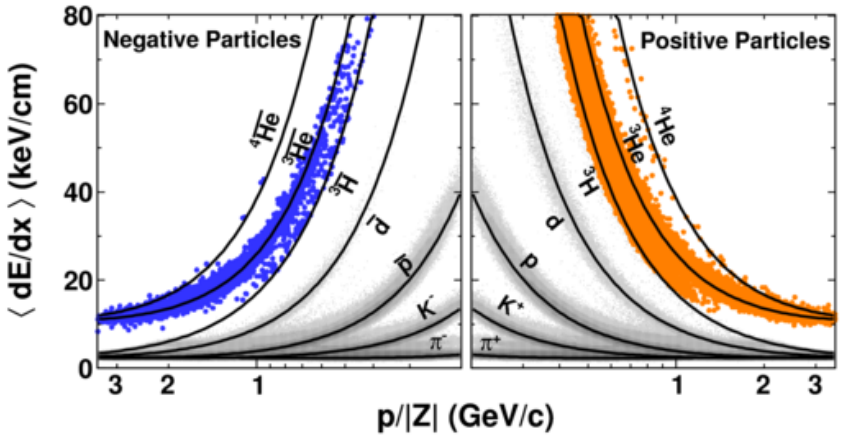

Figure 5.5: $\langle \mathrm{d}E/\mathrm{d}x \rangle$ versus $p/|Z|$ for antiparticles (left) and particles (right). Only data for $^3\overline{\mathrm{He}}$ (^{3}He) and $^4\overline{\mathrm{He}}$ (^{4}He) are included – represented by colour bands. Taken from Ref. [40].

with $B < -1$ are therefore rare product of such interactions.

The above conclusion can tell us more about nuclei (antinuclei) formation mechanism. Production through coalescence mechanism is thus favoured. Therefore nucleons (or hyperons) with low relative momenta and in proximity in phase space, i. e. both in position and momentum, can form bound states through simultaneous interaction.

Knowledge of antinuclei production mechanism can be very useful in looking for antimatter in far Universe. The Alpha Magnetic Spectrometer (AMS), installed at the International Space Station (ISS), is a cosmic ray detector which searches for distant galaxies made entirely of antimatter. The differential invariant yield for antihelium are $^3\overline{\mathrm{He}} \sim 10^{-6}$ and $^4\overline{\mathrm{He}} \sim 10^{-9}$ [40]. Production of antihelium in collisions of cosmic rays is therefore negligible. Any $\overline{\mathrm{He}}$ detected by AMS would be a strong evidence of antimatter sources in the Universe [38, 39].

5.2.2 Antihypertriton

Antihypertriton is a nucleus composed of antiproton, antineutron and antilambda hyperon. Recently, the STAR collaboration reported observation of about 70 antihypertritons $^3_{\Lambda}\overline{\mathrm{H}}$ [41].

The $^3_{\Lambda}\overline{\mathrm{H}}$ nucleus, created in primary vertex, cannot be directly measured. Therefore STAR seeks for its decay products. One of the possible decay channels is

$$^3_{\Lambda}\overline{\mathrm{H}} \rightarrow {}^3\overline{\mathrm{He}} + \pi^+.$$

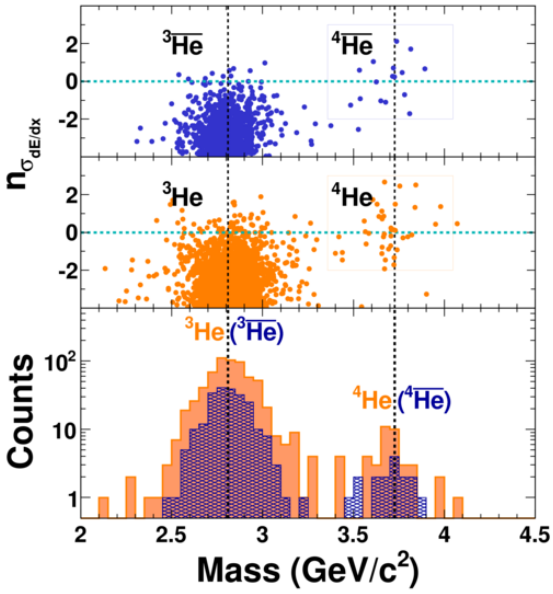

Figure 5.6: $\langle \mathrm{d}E/\mathrm{d}x \rangle$ (in units of multiples of CMS width of the energy loss per track distribution $\sigma_{\mathrm{d}E/\mathrm{d}x}$, $n_{\sigma_{\mathrm{d}E/\mathrm{d}x}}$) as a function of mass of the particle m measured by the ToF system. The first (second) panel shows negatively (positively) charged particles, the bottom panel shows mass distribution for all entries. The masses of ^{3}He ($^3\overline{\mathrm{He}}$) and ^{4}He ($^4\overline{\mathrm{He}}$) are indicated by vertical lines at $m = 2.81$ GeV/c^2 and $m = 3.73$ GeV/c^2 respectively. The horizontal line marks the position of zero deviation from the expected $\mathrm{d}E/\mathrm{d}x$ for ^{4}He ($^4\overline{\mathrm{He}}$). We see that most of the ^{4}He ($^4\overline{\mathrm{He}}$) entries are in the $\pm 3\sigma$ window, indicated by rectangular boxes. Taken from Ref. [40].

Such decay is pictured in Figure 5.8. The invariant mass of the candidate particle is calculated from the momenta of the two daughter particles. Obtained spectra can be found in Figure 5.9A (hypertriton) and Figure 5.9B (antihypertriton). The background is obtained from a track rotation method. Track of one of the daughter particles (in this case $^3\overline{\mathrm{He}}$ and ^{3}He) is rotated by π in azimuthal direction with respect to the event primary vertex. The rotated invariant mass distribution is then fit. Numbers of counts are determined by subtracting the rotated fit from the fit of all signal candidates. The observed amounts total 70 ± 17 for ${}^{3}_{\Lambda}\overline{\mathrm{H}}$ and 157 ± 30 for ${}^{3}_{\Lambda}\mathrm{H}$. Fig. 5.9C shows $\langle \mathrm{d}E/\mathrm{d}x \rangle$ versus rigidity $p/|Z|$ for negative tracks. Expected lines for $^3\overline{\mathrm{He}}$ and π are highlighted. Fig. 5.9D gives distributions for new variable z

$$z = \ln(\langle \mathrm{d}E/\mathrm{d}x \rangle / \langle \mathrm{d}E/\mathrm{d}x \rangle_B)$$

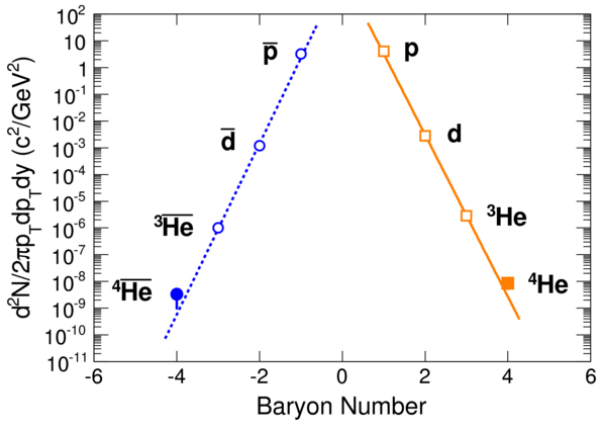

Figure 5.7: Differential invariant yields as a function of baryon number B, evaluated at $p_T/|B| = 0.875$ GeV/c, in central 200 GeV Au-Au collisions. Taken from Ref. [40].

where $\langle \mathrm{d}E/\mathrm{d}x \rangle_B$ is the expected value for the Bethe-Bloch formula for the given particle. Most of the $^3\overline{\mathrm{He}}$ and ^{3}He candidates are of $|z| < 0.2$. This implies the $^3\overline{\mathrm{He}}$ and ^{3}He are cleanly identified.

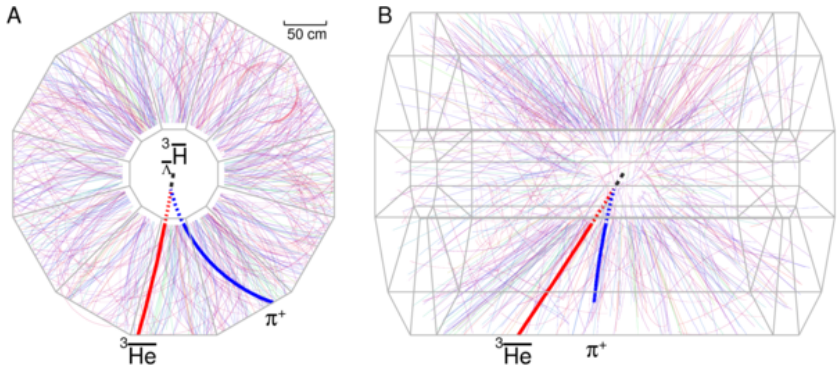

Figure 5.8: Visualisation of an event containing the decay ${}^3_{\bar{\Lambda}}\overline{\mathrm{H}} \rightarrow {}^3\overline{\mathrm{He}} + \pi^+$ recorded by STAR. Taken from Ref. [41].

Fitting the invariant mass distribution for ${}^3_{\bar{\Lambda}}\overline{\mathrm{H}}$ and ${}^3_{\Lambda}\mathrm{H}$ gives values of their mass

$$\begin{aligned} m({}^3_{\bar{\Lambda}}\overline{\mathrm{H}}) &= 2.991 \pm 0.001_{stat} \pm 0.002_{sys} \text{ GeV}/c^2 \\ m({}^3_{\Lambda}\mathrm{H}) &= 2.989 \pm 0.001_{stat} \pm 0.002_{sys} \text{ GeV}/c^2 \end{aligned} \tag{5.6}$$

.

The values are consistent not only one with another, but both are in good agreement with the best value from the literature

$$m(^3_\Lambda\mathrm{H}) = 2.99131 \pm 0.00005 \text{ GeV}/c^2,$$

published in [42] (according to [41]).

However, the decay products need to be properly identified. Figure 5.9C shows $\langle \mathrm{d}E/\mathrm{d}x \rangle$ versus magnetic rigidity $p/|Z|$ for negative particles. The measured energy loss $\langle \mathrm{d}E/\mathrm{d}x \rangle$ is then compared with the expected value for the given particle species and momentum, $\langle \mathrm{d}E/\mathrm{d}x \rangle_B$. New variable z is defined, $z = \ln\left(\langle \mathrm{d}E/\mathrm{d}x \rangle / \langle \mathrm{d}E/\mathrm{d}x \rangle_B\right)$. Figure 5.9D gives $z(^3\mathrm{He})$ distribution for $^3\mathrm{He}$ and $^3\overline{\mathrm{He}}$. The $^3\mathrm{He}$ and $^3\overline{\mathrm{He}}$ were clearly identifiable. Furthermore, distinct band of particles centering around the expected value for $^3\overline{\mathrm{He}}$ can be seen in graph 5.9C.

The production ratio $^3_{\bar{\Lambda}}\overline{\mathrm{H}}\ /^3_\Lambda\mathrm{H}$ is proportional to product of ratios for single composite antiparticles $\left(\frac{\bar{\Lambda}}{\Lambda} \times \frac{\bar{p}}{p} \times \frac{\bar{n}}{n}\right)$, which is consistent with the expectation that (anti)nuclei are formed through coalescence mechanism.

$$\begin{aligned} ^3_{\bar{\Lambda}}\overline{\mathrm{H}}\ /^3_\Lambda\mathrm{H} &= 0.45 \pm 0.18_{stat} \pm 0.07_{sys} \\ \left(\frac{\bar{\Lambda}}{\Lambda} \times \frac{\bar{p}}{p} \times \frac{\bar{n}}{n}\right) &= 0.45 \pm 0.08_{stat} \pm 0.10_{sys} \end{aligned} \tag{5.7}$$

The $^3_{\bar{\Lambda}}\overline{\mathrm{H}}$ lifetime τ is measured via the equation

$$N(t) = N(0)e^{-t/\tau} \tag{5.8}$$

where $t = lm/p$, l is the measured decay distance, p is the particle momentum and m its mass. In [41], the $^3_\Lambda\mathrm{H}$ and $^3_{\bar{\Lambda}}\overline{\mathrm{H}}$ samples were combined for better statistic, as the lifetimes of a particle and its antiparticle should equal. However, separate measurements were done, showing no difference within errors. The observed lifetime was

$$\tau = 182 \pm 89_{stat} \pm 27_{sys} \text{ ps} \tag{5.9}$$

The Λ hyperon lifetime was determined as an additional cross-check for the $\Lambda \longrightarrow p + \pi^+$ decay channel. Same data set and identical approach were used. The result is $\tau = 267 \pm 5_{stat}$ ps, which is consistent with the PDG value $\tau = 263 \pm 2$ ps [4].

5.3 Future perspectives on STAR

In the future, STAR will continue to look for exotics forms of matter and antimatter in several directions. To list a few fields of current and future research [43], STAR will look for possible heavier antimatter, such as $^4\overline{\mathrm{He}^*}$, $^4\overline{\mathrm{Li}}$ and $^5\overline{\mathrm{Li}}$, or for (anti)hypertriton with strangeness $S = 2 \vee 3$ ($pn\Xi^-$ and $pn\Omega^-$). The knowledge of SM can be pushed further by research in the field of strange particles. This involves search for H^0-dibaryon, either in form of strangelet - a

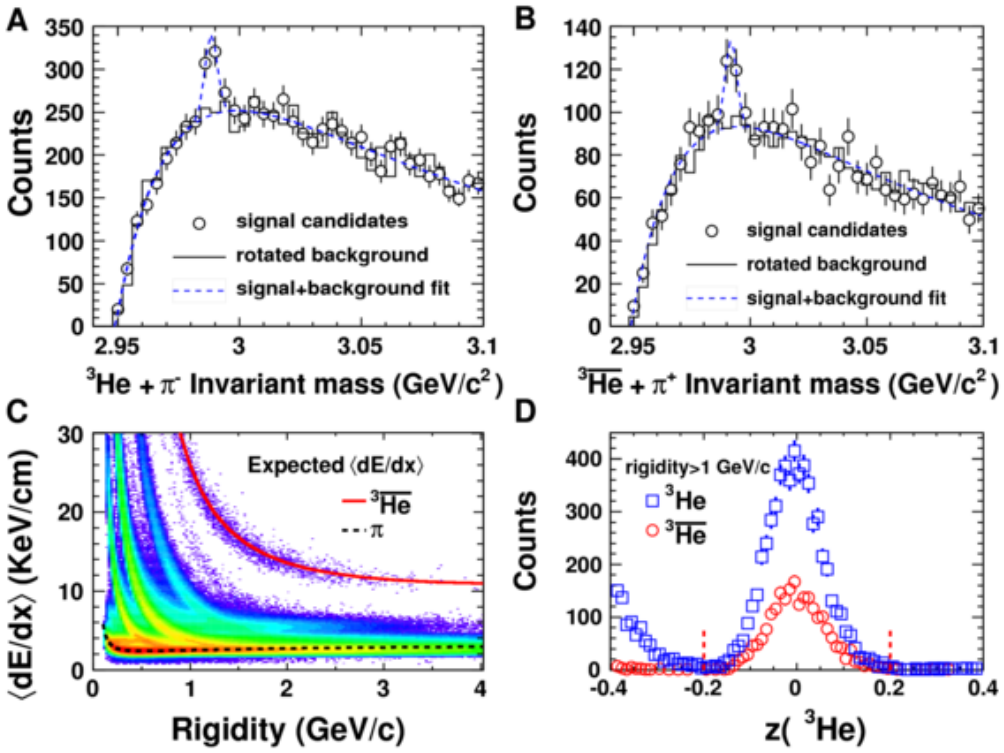

Figure 5.9: A: Invariant mass distribution of $^3\mathrm{He} + \pi^-$. B: Invariant mass distribution of $^3\overline{\mathrm{He}} + \pi^+$. C: $\langle \mathrm{d}E/\mathrm{d}x \rangle$ versus $p/|Z|$ for negative particles, expected values for $^3\overline{\mathrm{He}}$ and π tracks. D: $z = \ln(\langle \mathrm{d}E/\mathrm{d}x \rangle / \langle \mathrm{d}E/\mathrm{d}x \rangle_B)$ distribution for $^3\overline{\mathrm{He}}$ and ^{3}He candidates. Taken from Ref. [41].

quark-bag bound state (*uuddss*) - or as a bound state made by coalescence of two strange baryons.

Summary

The recent discoveries of exotic forms of antimatter at RHIC was discussed in this work with related subjects of antimatter, CP-violation, hypernuclei production.

Two experiments investigating properties of antihydrogen, AE$\bar{g}$IS and ALPHA at CERN, were discussed. Finally the details of the STAR experiment and observations of antihelium $^4\overline{\mathrm{He}}$, the heaviest antinucleus ever observed, as well as first observation of antihypernucleus ${}^3_{\Lambda}\overline{\mathrm{H}}$ were presented. In the future, STAR will pursue its search for exotic matter. It will focus on heavier antinuclei and continue its search for other forms of strange nuclei.

Bibliography

[1] Žáček, J.; Úvod do fyziky elementárních částic; Karolinum 2005, ISBN 80-246-1109-0.

[2] Perkins, D.; Particle Astrophysics; Oxford University Press 2009, 2nd edition, ISBN 978-0-19-954545-2.

[3] Úlehla, I.;Suk, M.;Trka, Z.; *Atomy, jádra a částice*, Academia 1990, ISBN 80-200-0135-2.

[4] Particle Data Group webpage; http://pdg.lbl.gov/.

[5] HyperPhysics - interactive physics exploration environment; webpage, url: hyperphysics.phy-astr.gsu.edu.

[6] Griffiths, D.; *Introduction to Elementary Particles*, John Willey & Sons, Inc. 1987, ISBN 0-471-60386-4.

[7] Close, F.; *Antimatter*, Oxford University Press 2009, ISBN 978-0-19-957887-0.

[8] Aubert, B. *et al.* (BaBar Collaboration); Phys. Rev. Lett **87** (2001) 091801.

[9] Abe, K. *et al.* (Belle Collaboration); Phys. Rev. Lett **87** (2001) 091802.

[10] Staric, M. *et al.* (Belle Collaboration); Phys. Rev. Lett **98** (2007) 211803.

[11] Aubert, B. *et al.* (BaBar Collaboration); Phys. Rev. D **80** (2009) 071103.

[12] Aubert, B. *et al.* (BaBar Collaboration); Phys. Rev. Lett **98** (2007) 211802.

[13] Aaij, R. *et al.* (LHCb Collaboration); JHEP **1204** (2012) 129.

[14] Vogt, R.; *Ultrarelativistic Heavy-Ion Collisions*, Elsevier 2007, ISBN 978-0-444-52196-5.

[15] Anderson, C. D.; Phys. Rev. **43**(1933) 491.

[16] Chamberlain, O. *et al.*; Phys. Rev. **100**(1955) 947.

[17] Cork, B. *et al.*; Phys. Rev. **104** (1956) 1193.

[18] Baur, G. *et al.*; Phys. Lett. B **368** (1996) 251.

[19] Alberico, W. M.; Garbarino, G.; Phys. Rep **369** (2002) 1.

[20] Wróblewski, A. K.; Acta Physica Polonica B **35** (2004), 893.

[21] Bydžovský, P.; Topics in Strangeness Nuclear Physics, Springer 2007, ISBN 978-3-540-72038-6.

[22] Zenoni, A. and Gianotti, P.; Europhysics News **33** (2002) 157.

[23] Agnello, M. *et al.* (FINUDA Collaboration), Phys. Rev. Lett. **108** (2012) 042501.

[24] Butler, E.; PhD Thesis, Swansea University, 2011.

[25] Fajans, J.; Schmidt, A.; AIP Conf. Proc. **692** (2003) 252.

[26] Antiproton Decelerator CERN; retrieved 17-06-2012 from Wikimedia Commons,
url: http://commons.wikimedia.org/wiki/File:Antiproton_Decelerator_CERN.svg.

[27] Penning trap, retrieved 16-05-2012 from AIP Physics News Graphics
url: http://www.aip.org/png/html/penning.htm.

[28] Hellemans, A.; Nature **406** (2000) 556.

[29] Nielsen, M.; Phil. Trans. R. Soc. A **368** (2010) 3671.

[30] Andresen, G. B. *et al.* (ALPHA Collaboration), Nature **468** (2010) 673.

[31] Andresen, G. B. *et al.* (ALPHA Collaboration), Nature Physics **7** (2011) 558.

[32] Amole, G. *et al.*; Nature **483** (2012) 439.

[33] The AEGIS/AD-6 Collaboration; CERN-SPSC-2011-007/SPSC-SR-096.

[34] Testera, G. *et al.*; AIP Conf. Proc. **1037** (2008) 5.

[35] AE$\bar{g}$IS webpage; url: http://aegis.web.cern.ch/aegis/home.html.

[36] Baumgart, S.; PhD Thesis, Yale University, 2009.

[37] Anderson, M. *et al.*; Nucl. Instrum. Meth. A **499** (2003) 659.

[38] Alpha Magnetic Spectrometer webpage; url: http://www.ams02.org/.

[39] NASA Science News webpage;
url: http://science.nasa.gov/science-news/science-at-nasa/2009/14aug_ams/.

[40] Agakishiev, H. *et al.*; Nature **473** (2011) 353.

[41] Abelev, B. I. *et al.*; Science **328** (2010) 58.

[42] Juric, M. *et al.*; Nucl. Phys. B **52** (1973) 1.

[43] Tang, A.;*Future Perspectives on STAR Exotic Searches*, Workshop On Hyperon-Hyperon Interactions and Searches for Exotic Di-Hyperons in Nuclear Collisions, BNL February 29 – March 2 2012.

[44] The STAR experiment at the Relativistic Heavy-Ion Collider, Brookhaven National Laboratory, webpage; http://www.star.bnl.gov/.